

# Designing Thieno[3,4-c]pyrrole-4,6-dione Core-Based, $A_2-D-A_1-D-A_2$ -Type Acceptor Molecules for Promising Photovoltaic Parameters in Organic Photovoltaic Cells

Tanzeela Noor, Muhammad Waqas, Mohamed Shaban, Shanza Hameed, Ateeq-ur-Rehman, Samia Ben Ahmed,\* H. A. Alrafai, Sameerah I. Al-Saeedi, Mahmoud A. A. Ibrahim, N. M. A. Hadia, Rasheed Ahmad Khera,\* and Abeer A. Hassan\*



Cite This: *ACS Omega* 2024, 9, 6403–6422



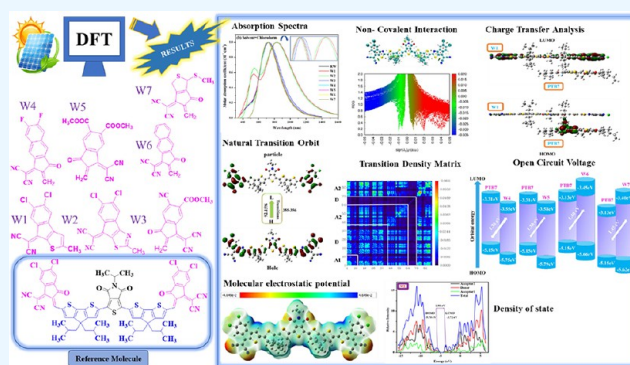
Read Online

ACCESS |

Metrics & More

Article Recommendations

**ABSTRACT:** Nonfullerene-based organic solar cells can be utilized as favorable photovoltaic and optoelectronic devices due to their enhanced life span and efficiency. In this research, seven new molecules were designed to improve the working efficiency of organic solar cells by utilizing a terminal acceptor modification approach. The perceived  $A_2-D-A_1-D-A_2$  configuration-based molecules possess a lower band gap ranging from 1.95 to 2.21 eV compared to the pre-existing reference molecule (RW), which has a band gap of 2.23 eV. The modified molecules also exhibit higher  $\lambda_{\max}$  values ranging from 672 to 768 nm in the gaseous and 715–839 nm in solvent phases, respectively, as compared to the (RW) molecule, which has  $\lambda_{\max}$  values at 673 and 719 nm in gas and chloroform medium, respectively. The ground state geometries, molecular planarity parameter, and span of deviation from the plane were analyzed to study the planarity of all of the molecules. The natural transition orbitals, the density of state, molecular electrostatic potential, noncovalent interactions, frontier molecular orbitals, and transition density matrix analysis of all studied molecules were executed to validate the optoelectronic properties of these molecules. Improved charge mobilities and dipole moments were observed, as newly designed molecules possessed lower internal reorganization energies. The open circuit voltage ( $V_{oc}$ ) of W4, W5, W6, and W7 among newly designed molecules was improved as compared to the reference molecule. These results elaborate on the superiority of these novel-designed molecules over the pre-existing (RW) molecule as potential blocks for better organic solar cell applications.



## 1. INTRODUCTION

Organic solar cells (OSCs) have gained prominence in power generation over the past few decades due to their higher mechanical flexibility, lower cost, lighter weight, and simplicity of processing in the form of solution.<sup>1,2</sup> The essential elements of OSCs include negative and positive electrodes, an electron and hole transportation layer, and an active layer of organic materials that act as incident light-absorbing materials.<sup>3</sup> The bulk–heterojunction active layer formed by combining acceptor materials, exhibiting high electron affinity, with donor materials with a low ionization potential, appears to be the most effective active layer so far.<sup>4</sup> Due to the greater donor/acceptor interfacial area and the smaller exciton diffusion range afforded through this arrangement, the light response was increased.<sup>5–8</sup>

Recently, bulk heterojunction OSCs based on nonfullerene acceptors have significantly increased power conversion

efficiency. Nonfullerene acceptors (NFAs) have conveniently tunable energy levels, easy fabrication, and great visible absorptivity and are considerably less expensive than fullerene acceptors. Because of fast advances in the design of NFA molecules, their efficiency (up to 20% for tandem solar cells) has already overtaken that of FA-based OSCs.<sup>9,10</sup>

Fused-ring electron acceptors (FREAs) are distinguished among NFAs in this research area. However, their high production cost and significant synthetic complexity restrict their synthesis and commercialization. That is why nonfused

Received: July 31, 2023

Revised: January 12, 2024

Accepted: January 17, 2024

Published: February 2, 2024



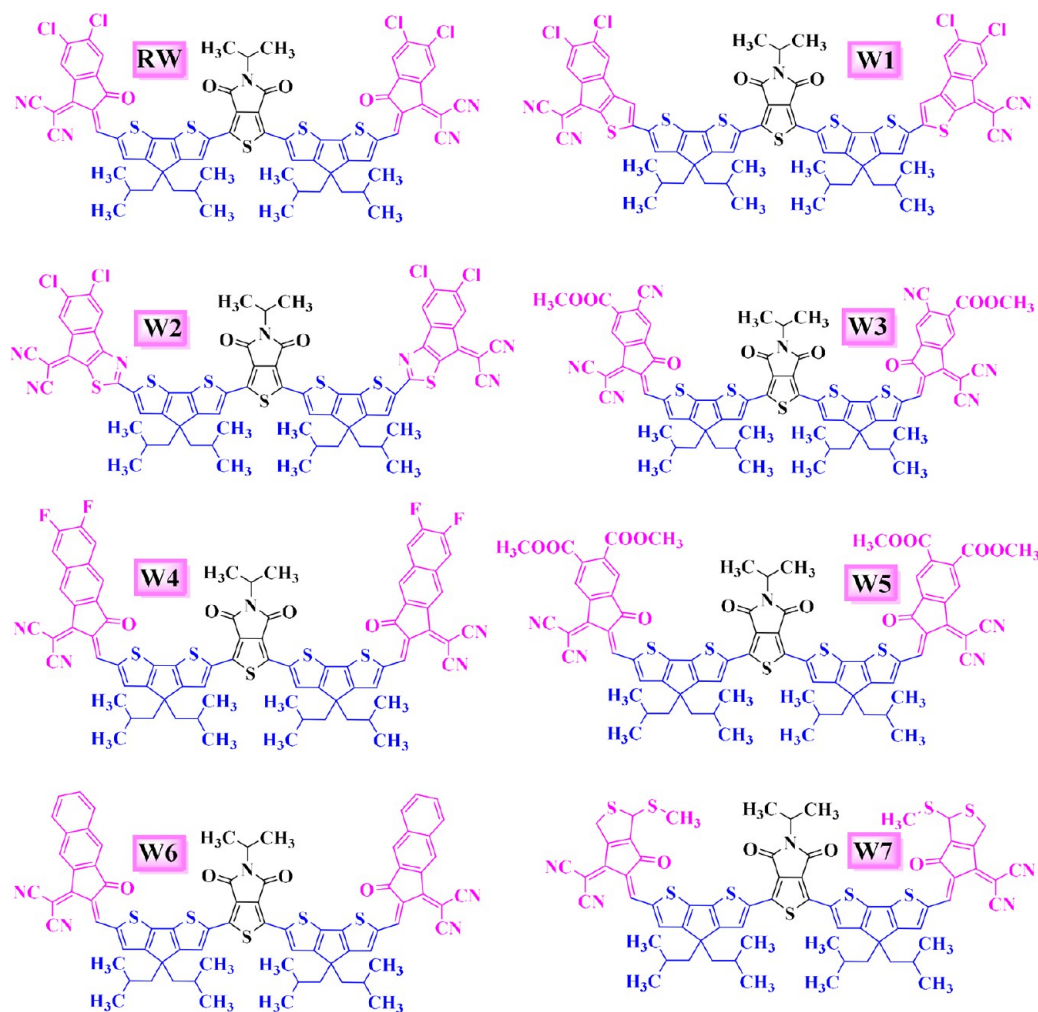


Figure 1. Chemical structure of W-shaped RW and W1–W7 molecules.

ring electron acceptors (NFREAs) are the center of attention because they are affordable and need more straightforward synthesis steps than FREAs.<sup>11,12</sup> Fused-ringed structures are more challenging to construct than structures connected through a single bond, which can be produced at a lower cost and with a lower synthetic complexity. Furthermore, it is also possible to fine-tune the NFREAs' absorption spectra and energy levels.<sup>13–16</sup>

Various molecular design strategies have been developed to tune the energy levels for easy charge transfer and improve OSC efficiency, such as end-capped modification, spacer insertion, and side-chain engineering.<sup>17–20</sup> The literature review reveals that the terminal acceptors' transformation played an important role.<sup>21,22</sup> An efficient alteration of PC<sub>70</sub>BM by substituting a visible light-absorbing cyano vinylene-4-nitrophenyl segment for the methyl group resulted in CN-PC<sub>70</sub>BM. CN-PC<sub>70</sub>BM showed stronger absorption ranging from 350 to 550 nm with improved PCE up to 4.88%.<sup>23</sup> In another attempt, the fill factor of CN-PC<sub>70</sub>BM was improved to 0.689 from 0.488, and PCE was improved to 8.2%.<sup>24</sup>

C8C8–4Cl is a recently synthesized nonfused ring electron acceptor (NFREA), which shows absorption at 728 nm in CHCl<sub>3</sub> and at 780 nm in a neat film. It has a bandgap of 1.41 eV, having HOMO at –5.70 eV and LUMO at –4.30 eV. Furthermore, it exhibits a good PCE of 13.96%, high fill factor

(71.10%), significant  $V_{oc}$  of 0.81 V, and prominent short circuit current value of 23.43 mA cm<sup>–2</sup>. The overall topology of the molecule is A<sub>2</sub>–D–A<sub>1</sub>–D–A<sub>2</sub> (A<sub>2</sub> represents terminal acceptors, D represents donor, and A<sub>1</sub> represents central acceptor) type, which contains 2-(5,6-Dichloro-2-ethylidene-3-oxo-indan-1-ylidene)-malononitrile as terminal acceptors, (4,4-Diisobutyl-2-methyl-4H-cyclopenta[2,1-b;3,4-b']dithiophene) as the donor part, and (5-(1-Ethyl-propyl)-thieno[3,4-c]-pyrrole-4,6-dione) as the central acceptor.<sup>13,25</sup> We can substitute this molecule's donor and acceptor parts to modify the photovoltaic and optoelectronic attributes.<sup>26–28</sup>

In this study, terminal acceptors (A<sub>2</sub>) of C8C8–4Cl (reference molecule mentioned as RW) are modified by seven new acceptor moieties, including 2-(5,6-dichloro-2-methyl-1-thia-cyclopenta[a]inden-8-ylidene)-malononitrile (W1), 2-(5,6-dichloro-2-methyl-indeno[1,2-d]thiazol-8-ylidene)-malononitrile (W2), 6-cyano-3-dicyanomethylene-2-methylene-1-oxo-indan-5-carboxylic acid methyl ester (W3), 2-(6,7-difluoro-2-methylene-3-oxo-2,3-dihydro-cyclopenta[b]-naphthalen-1-ylidene)-malononitrile (W4), 1-dicyanomethylene-2-methylene-3-oxo-indan-5,6-dicarboxylic acid dimethyl ester (W5), 2-(2-methylene-3-oxo-2,3-dihydro-cyclopenta[b]-naphthalen-1-ylidene)-malononitrile (W6), and 2-(5-methylene-1-methylsulfanyl-6-oxo-1,3,5,6-tetrahydro-cyclopenta[c]-thiophen-4-ylidene)-malononitrile (W7). The terminal acceptors with excellent electron-withdrawing abilities cause red-

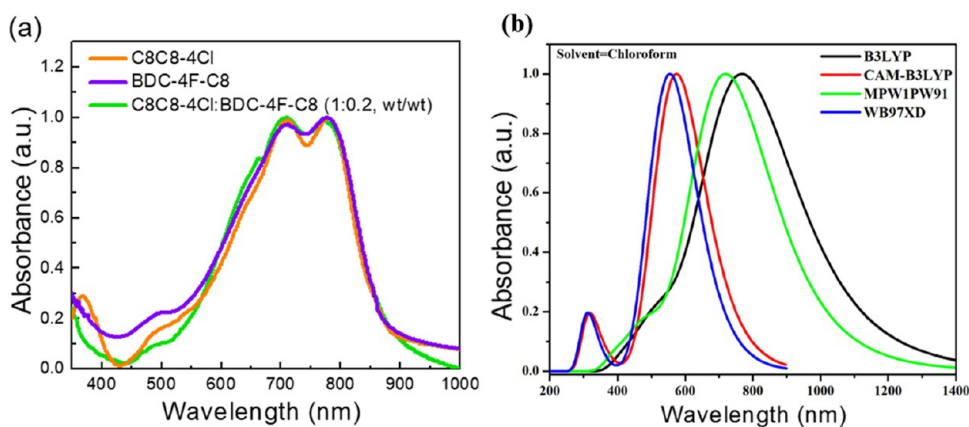


**Figure 2.** (a) Experimentally observed  $\lambda_{\max}$  of C8C8-4Cl in solvent medium and  $\lambda_{\max}$  of C8C8-4Cl with four different functionals of TD-DFT (b).

shifted absorption, reduced band gap, and enhanced charge transfer, leading to improved optoelectronic capabilities of the molecules. In this regard, different terminal acceptors were employed in order to notice the effect of increased conjugation on the photovoltaic performance. This study is very promising in explaining the nature of these acceptor moieties in practical applications of OSCs.<sup>29</sup> The molecular sketches of modified molecules (W1–W7) along with the reference molecule are shown in Figure 1.

## 2. COMPUTATIONAL DETAILS

All computational studies were performed using the Gaussian 09<sup>30</sup> software. Initially, we used GaussView 6.0<sup>31</sup> to design computationally processable geometry of the reference molecule. We employed the restricted spin on four particular integrals, namely, B3LYP,<sup>32,33</sup> CAM-B3LYP,<sup>34</sup> MPW1PW91,<sup>35</sup> and WB97XD,<sup>36</sup> at a basis set of 6-31G(d,p). The spin was restricted to prevent any spin contamination of the simulation result. The DFT technique was utilized for the optimization of the molecular structures. The polarizable continuum model (PCM) and its integral equation formalism variant (IEFPCM) were used to obtain their ultraviolet–visible absorption peaks in the solvent medium using the TD-DFT approach.<sup>37</sup> The calculations were performed at restricted spin at 10 different excited states. The charge of the system was kept neutral during the processing of these calculations. The solvent used in this research was chloroform. To determine which functional might be most appropriate for additional computations, the highest absorption wavelength ( $\lambda_{\max}$ ) of RW with the four functionals<sup>38</sup> stated above was contrasted to the experimental  $\lambda_{\max}$  of RW from published data (728 nm). The obtained  $\lambda_{\max}$  values were 770, 574, 719, and 554 nm from B3LYP, CAM-B3LYP, MPW1PW91, and WB97XD, respectively. From Figure 2, it is revealed that the MPW1PW91 (719 nm) functional showed the nearest  $\lambda_{\max}$  value with a difference of 9 nm from the experimental value. Therefore, the MPW1PW91 functional was selected for further analysis. The structural optimization of all the designed structures was performed by utilizing selected functional at the 6-31G(d,p) basis set.

The frontier molecular orbital analysis values were viewed by employing GaussView 6.0 software. Their absorption spectra were plotted utilizing Origin 6.0 software.<sup>39</sup> The density of state (DOS) graph was drawn using the PyMolyze 1.1 program.<sup>40,41</sup> However, transition density matrix (TDM) graphs were plotted using Multiwfn 3.7 software.<sup>42,43</sup> The

reorganization energy data of holes ( $\lambda_h$ ) and electrons ( $\lambda_e$ ) were analyzed by using eqs 1 and 2.<sup>44</sup>

$$\lambda_e = [E_-^0 - E_0] + [E_0^- - E_-] \quad (1)$$

$$\lambda_h = [E_+^0 - E_0] + [E_0^+ - E_+] \quad (2)$$

Here, an optimized neutral molecule attains the energies at cationic, anionic, and neutral states. The  $E_-^0$  and  $E_-$  are the energies at neutral and anionic forms obtained from optimized anionic molecules. Finally,  $E_+^0$  and  $E_+$  are energies at neutral and cationic states acquired from the optimized cationic molecules. The geometries of cation and anion elaborate the charge transition from the donor to the acceptor part of the molecule.<sup>45,46</sup>

## 3. RESULTS AND DISCUSSION

**3.1. Molecular Geometries.** All the designed molecules were optimized to study the geometrical and structural properties utilizing the MPW1PW91/6-31G(d,p) theory level in Gaussian 9.0 software.<sup>47</sup> All the studied molecules have the same central acceptor, i.e., 5-(1-ethyl-propyl)-thieno[3,4-*c*]-pyrrole-4,6-dione, and donor, i.e., (4,4-diisobutyl-2-methyl-4H-cyclopenta[2,1-*b*;3,4-*b'*]dithiophene), but they have different terminal acceptor groups, as shown in Figure 3. Therefore, studying the geometrical properties of the parts that differ among all molecules is essential. Optimized geometry plays a vital role in determining the stability of molecules, self-aggregation, and movement of charges in the molecule.<sup>48</sup>  $\Phi$  and  $L_b$  represent the dihedral angle and bond length between the successive carbon atoms of the terminal acceptor and donor part. These were examined to view the studied molecules' structural optimization, planarity, and conjugation, as shown in Figure 3. For understanding, Table 1 concludes the bond length and dihedral angle values of reference and proposed compounds.

The dihedral angle gives us a view of the optimization extent and the molecule's conjugation. Higher values of the dihedral angles represent that molecules have 3D geometry with the least planarity.<sup>49</sup> Smaller dihedral angle values will lead toward true structural planarity, which assists in charge transfer by conjugation and facilitates self-aggregation.<sup>50</sup> The dihedral angle on the donor and terminal acceptor's left and right sides is represented with  $\Phi_1$  and  $\Phi_2$ , respectively. The dihedral angle values on both sides of the reference molecule are 0.007° and 0.006°, which elaborate the planar geometry of the molecule. It is clear from Table 1 that all of the studied

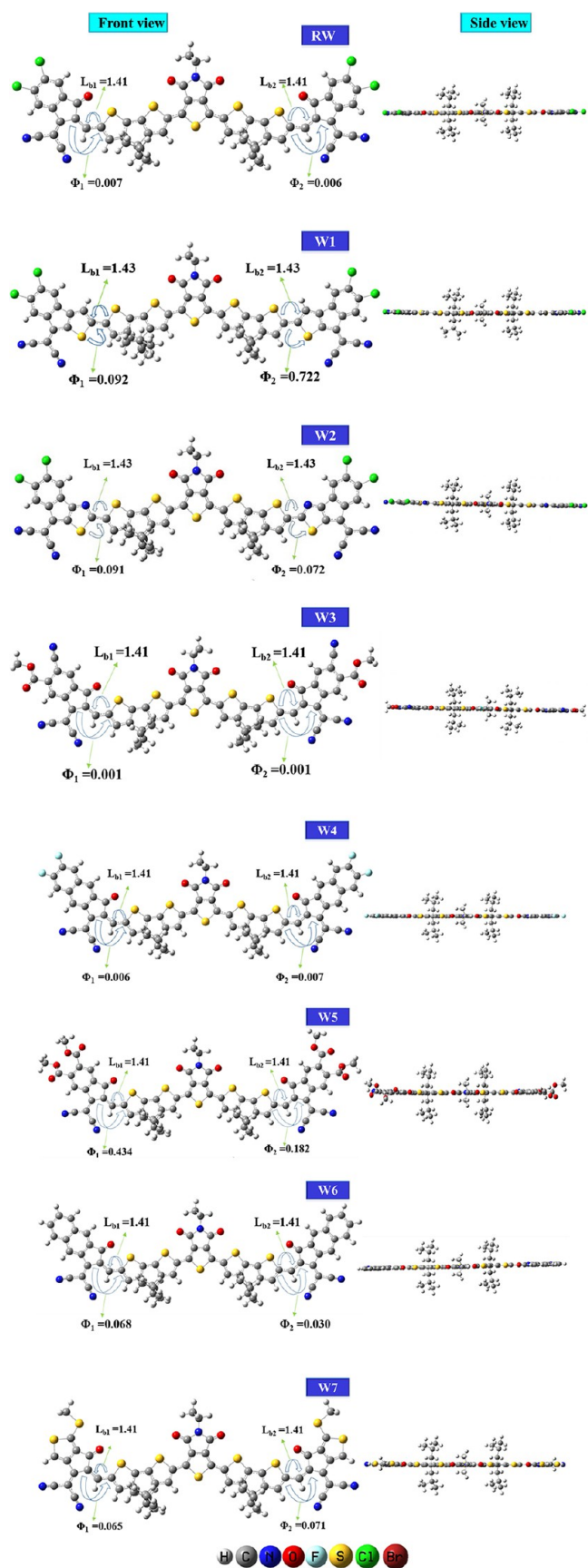


Figure 3. Optimized structure of C8C8–4Cl and W1–W7 molecules.

Table 1. Bond lengths and dihedral angles of RW and W1–W7

molecules	bond length ( $L_{b1}$ )	bond length ( $L_{b2}$ )	$\Phi_1$	$\Phi_2$
RW	1.41	1.41	0.007	0.006
W1	1.43	1.43	0.092	0.722
W2	1.42	1.42	0.091	0.072
W3	1.41	1.41	0.001	0.001
W4	1.41	1.41	0.006	0.007
W5	1.41	1.41	0.434	0.182
W6	1.41	1.41	0.068	0.030
W7	1.41	1.41	0.065	0.071

molecules (W1–W7) have rough similarities present between the dihedral angle values on both calculated sites which elaborates their planner structure. The range of the dihedral angle of all of the molecules is from  $0.006^\circ$  to  $0.434^\circ$ . All molecules have dihedral angle values close to zero, which elaborates their minute deviation from the planarity; this may occur due to steric hindrance produced by bulky terminal acceptor groups.

The calculated bond length values of ( $L_{b1}$  and  $L_{b2}$ ) between the donor and terminal acceptors range from 1.41 to 1.43 Å. These values lie within the range of single and double (C–C) bond lengths, elaborating the presence of conjugation due to the delocalization of the Pi-bond between them. Since the molecules' central acceptor ( $A_1$ ) and donor groups are the same, the minute variations in bond lengths are due to different terminal acceptor groups ( $A_2$ ). The different acceptors with excellent electron-withdrawing abilities lead toward higher conjugation and shorter bond lengths.<sup>51</sup> All molecules represent nearly the same bond length values (1.41 Å) between terminal acceptors and donor groups, except the W1 and W2 molecules, having bond length values of 1.43 Å, representing more conjugation in these molecules.

**3.2. Planarity Analysis.** The molecular planarity parameters (MPP) and span of deviation from the plane (SDP) investigations were performed to analyze the planarity of the studied molecules. MPP gives an analysis of the deviation of atoms from the plane. However, SDP analysis provides structural parts' deviation from the fitted plane.<sup>52</sup> The molecule with lower values of MPP and SDP elaborates on the planar structure and high conjugation present in that molecule. Moreover, maximum negative deviation (MND) and maximum positive deviation (MPD) values are examined to visualize which atoms represented the highest positive and negative deviation from the whole molecular plane (shown in Figure 4).<sup>52</sup> The results of all of the analyzed parameters are tabulated in Table 2.

The calculated MPP values of the RW and W1–W7 molecules, except W5, lie in the range  $0.0006$ – $0.0595$  Å, suggesting the planar structures of these molecules. W3 represents the most planarity compared to other studied molecules due to the smallest MPP ( $0.0006$  Å) and SDP values ( $0.0067$  Å). However, the highest MPP and SDP values of the W5 molecule represent the highest deviation from the plane that resulted in minimizing the steric repulsion between ester moieties of the terminal acceptors. The MPP and SDP values of W6 are slightly less than those of W7, representing that W6 has a more planar structure than W7. Compared to RW, the W4 molecule exhibits a marginally higher SDP value due to the electronegative fluorine atoms in the  $A_2$  acceptor region of this

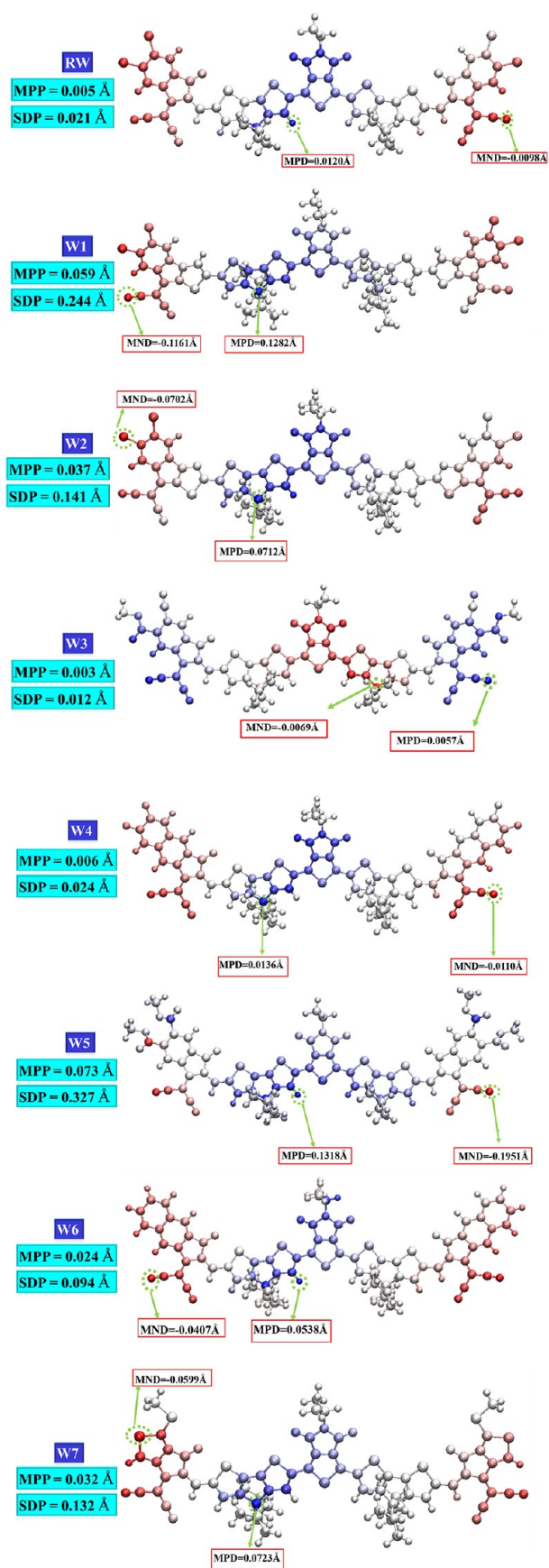


Figure 4. Structures showing the planarity parameters of RW and W1–W7 molecules.

Table 2. Calculated values of MPP, SDP, MPD, and MND of RW and W1–W7 molecules

molecules	MPP (Å)	SDP (Å)	MPD (Å)	MND (Å)
RW	0.0058	0.0218	0.0120	−0.0098
W1	0.0595	0.2444	0.1282	−0.1161
W2	0.0371	0.1415	0.0702	−0.0712
W3	0.0034	0.0126	0.0057	−0.0069
W4	0.0062	0.0247	0.0136	−0.0110
W5	0.5332	3.8155	1.7947	−2.0207
W6	0.0241	0.0945	0.0538	−0.0407
W7	0.0325	0.1322	0.0723	−0.0599

chromophore. This describes the minute structural deviation of W4 from the plane compared with the RW molecule.

The devised structures are represented with blue, silver, and red colors. The blue color elaborates the positive deviation from the plane, and the red color elaborates the negative deviation from the plane. The color density represents the degree of deviation from the plane. The calculated MND and MPD values of the RW and W1–W7 molecules are tabulated in Table 2.

The MND and MPD values provide information about the atom representing maximum positive and negative deviations from the plane as concerned with the whole molecule. In the terminal acceptors, the nitrogen atoms of RW, W1, W2, W4, W5, and W6, along with the sulfur atoms of W7, represent the maximum negative deviation. In comparison, the maximum positive deviation is shown by carbon and hydrogen atoms in all molecules. The atoms representing the highest MND and MPD are highlighted with an arrow in Figure 4.

**3.3. Frontier Molecular Orbital Analysis.** The analysis of the highest occupied molecular orbital (HOMO) and lowest unoccupied molecular orbitals (LUMO) gives us an overview of the probability of charge transfer from the ground state to the excited state in organic solar cells.<sup>53</sup> FMOs assist us in qualitatively evaluating the bonding character of the orbitals, which is responsible for the electronic transitional changes for each pair of bonded atoms. By capturing photons from the sunlight, OSC causes the electronic transitions from HOMO orbital to LUMO orbital due to the movement of electrons from a lower energy ground state to a higher energy excited state.<sup>54</sup> The band gap indirectly affects these electronic excitations, affecting the photovoltaic properties, excitation energies, charge density, and absorption spectra of molecules. The increase in the band gap value results in less charge transfer in chromophores.<sup>55</sup> Higher HOMO concentration on the donor part and LUMO concentration on the acceptor part assist in charge transfer toward end-capped acceptors by excitations.<sup>56</sup>

Electron delocalization is also highly influenced by the electronegativity of atoms in molecules. The electronegativity of atoms within a molecule can lead to variations in the energy levels of HOMO and LUMO. This energy level tuning can impact the efficiency of charge transfer processes in organic solar cells. More electronegative atoms will have lower energy orbitals, which can lead to more delocalization of electrons.<sup>57,58</sup> The band gap values between HOMO and LUMO energy levels were calculated utilizing eq 3.

$$E_g = E_{\text{LUMO}} - E_{\text{HOMO}} \quad (3)$$

The HOMO–LUMO energy values and their concerned band gap values are tabulated in Table 3, and charge density

**Table 3.**  $E_{\text{HOMO}}$ ,  $E_{\text{LUMO}}$ , and energy gap ( $E_g$ ) of RW and W1–W7

molecules	$E_{\text{HOMO}}$ (eV)	$E_{\text{LUMO}}$ (eV)	$E_g$ (eV)
RW	−5.86	−3.63	2.23
W1	−5.58	−3.63	1.95
W2	−5.70	−3.72	1.98
W3	−5.94	−3.76	2.18
W4	−5.75	−3.55	2.20
W5	−5.79	−3.58	2.21
W6	−5.66	−3.45	2.21
W7	−5.62	−3.40	2.22

distribution is shown in Figure 5. The regions having positive potential are symbolized by the red-colored lobe. In contrast, the green color lobe represents the negative potential regions.<sup>59</sup> HOMO charge density is mainly present on the designed chromophores' central acceptor and donor region (except W1 and W2). However, the LUMO charge density is spread throughout the molecular structure. In W1 and W2 molecules, the LUMO density is mainly present on the  $A_2$  acceptors of these molecules due to the lower band gap. These molecules efficiently transfer charge from the donor region to the acceptor  $A_2$  region. The performance, working capability, and efficiency of OSCs are directly related to their HOMO and LUMO energy levels.

The tabulated data show that the RW molecule's band gap is 2.23 eV, exhibiting HOMO at 5.86 eV and LUMO at 3.63 eV. In contrast to RW, W3 has a low-lying HOMO energy value (−5.95 eV), while HOMO energy values for W1, W2, W4, W5, W6, and W7 are −5.58, −5.70, −5.75, −5.79, −5.66, and −5.62 eV. In terms of LUMO energy levels, all the designed molecules (except W2 and W3) have high-lying values than RW, i.e., −3.63 eV for W1, −3.55 eV for W4, −3.58 eV for W5, −3.45 eV for W6, and −3.40 eV for W7. It represents that newly designed molecules are efficient acceptor materials that could be blended with donor material. All recently perceived molecules represent lower band gap values than RW. The increasing band gap order of scrutinized molecules is  $W1 < W2 < W3 < W4 < W5 = W6 < W7 < RW$  having values of 1.95, 1.98, 2.18, 2.20, 2.21, 2.21, 2.22, and 2.23 eV, respectively. The W1 and W2 molecules represent the highest decrease in band gap due to the presence of 2-(5,6-dichloro-1-thia-cyclopenta[a]inden-8-ylidene)-malononitrile and 2-(5,6-dichloro-indeno[1,2-d]thiazol-8-ylidene)-malononitrile-type terminal acceptor ( $A_2$ ) moieties. These moieties resulted in the efficient pulling of electrons toward these molecules' terminal -Cl atoms.

By comparing the structure of W3 and W5, these two molecules have similar acceptors with slight differences; the acceptor of W5 has four COOCH<sub>3</sub> groups on their end side, while W3 has two CHOOCH<sub>3</sub> groups and two CN cyanide groups, which have more electron-withdrawing capabilities than the COOCH<sub>3</sub> group on terminal acceptors, causing more reduction in energy gap in W3 as compared to W5. Acceptors of W4 and W6 also have similar structures, but W4 has four electron-withdrawing fluorine atoms on the terminal acceptors, causing more band gap reduction than W6, which has no fluorine atoms. The reduced band gap of W6 as compared to RW is due to the balanced molecular energy levels, i.e., its molecular energy levels are not too high or low lying, causing a narrow band gap.<sup>60</sup> Moreover, these groups with prominent electron-withdrawing abilities lead to better charge separation

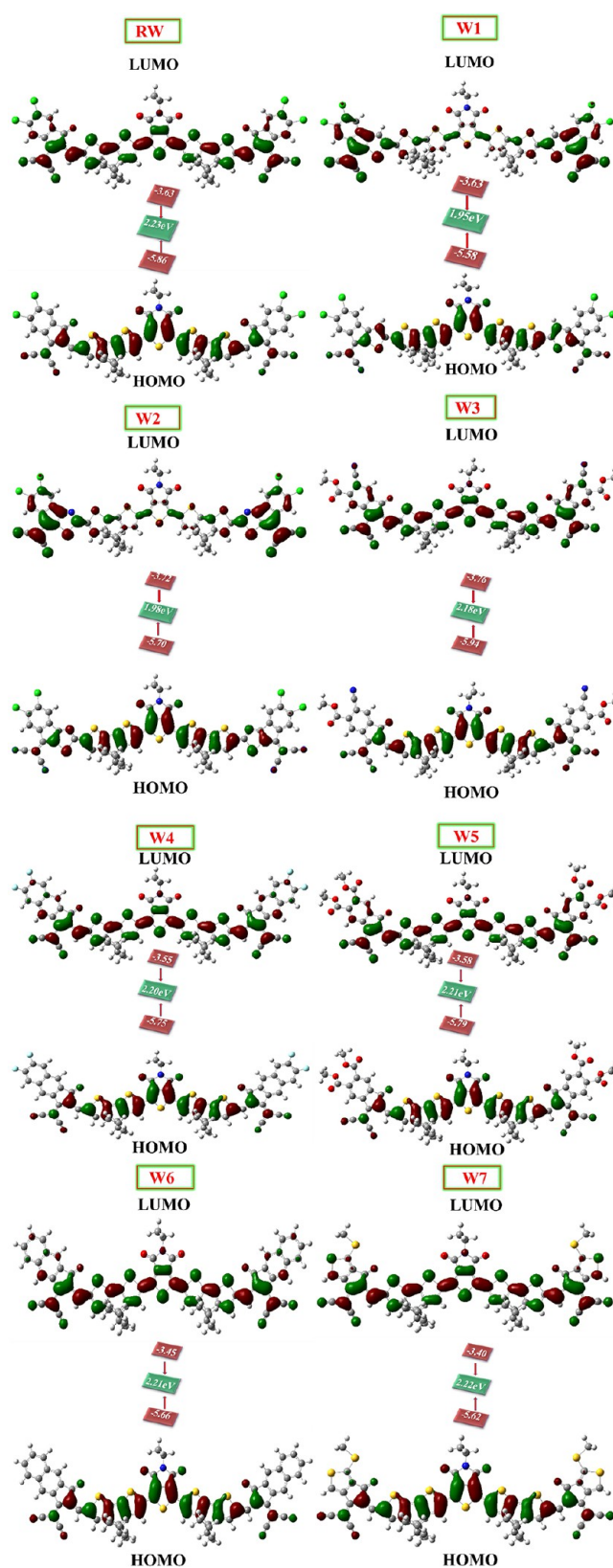


**Figure 5.** Frontier molecular orbitals (FMOs) of RW and W1–W7 molecules.

and enhanced photovoltaic absorption properties of these chromophores. Other scrutinized molecules also exhibit a reduction in band gap values compared with RW, resulting in convenient charge transition in light of the band theory of

energy. This reveals that these perceived chromophores are good opportunities to be used as proficient OSCs.

Quantum chemical studies of the organic compound are essential parameters to evaluate the charge transfer properties of OSCs for their practical uses. Ionization potentials and electron affinities are related to the HOMO and LUMO energies, respectively. They are vital factors in the stability index of molecules that indicate the molecule's chemical reactivity.<sup>61</sup> The ionization potentials (IP) and electron affinities (EA) of the molecule can act as a critical reference for molecular design to calculate the holes/electrons transport barriers of the active layer in the OSCs.<sup>62</sup> Chromophores with high EA and low IP values accelerate the charge transfer process. A larger EA facilitates the injection of electrons into vacant LUMO, and a minor IP could decrease the barrier for injecting holes.<sup>63</sup> The values of IP and EA are calculated from eqs 4 and 5<sup>64</sup> listed in Table 4.

$$\text{IP} = [E_0^+ - E_0] \quad (4)$$

$$\text{EA} = [E_0 - E_0^-] \quad (5)$$

**Table 4. Representation of Ionization Potential (IP), Electron Affinity (EA), Softness, and Hardness ( $\eta$ ) of RW and W1–W7**

molecules	IP (eV)	EA (eV)	softness (S)	hardness ( $\eta$ )
RW	6.51	2.99	0.28	1.76
W1	6.14	2.93	0.31	1.61
W2	6.27	2.97	0.30	1.65
W3	6.60	3.13	0.29	1.73
W4	6.40	2.93	0.29	1.73
W5	6.45	2.94	0.29	1.75
W6	6.30	2.81	0.29	1.74
W7	6.43	2.75	0.27	1.84

Among the studied molecules, the W1 molecule has the lowest IP value (6.14 eV) because W1 has a high-lying energy value of HOMO (−5.58 eV) among the proposed molecules. In contrast, the W3 molecule has the highest IP value (6.60 eV) due to a low-lying HOMO energy value of −5.95 eV. The W3 molecule has the highest value of EA (3.13 eV) among all molecules because of its low LUMO value at −3.77 eV.

The primary characteristics of global hardness and softness are intended to impact and provide a quantitative description of the molecular reactivity and chemical stability significantly. The correlation between chemical hardness and softness and IP and EA could be seen from eqs 6 and 7.<sup>65–67</sup>

$$\eta = (\text{IP} - \text{EA})/2 \quad (6)$$

$$S = 1/(2\eta) \quad (7)$$

Here, " $\eta$ " represents the chemical hardness, and "S" represents the softness of the molecule. IP corresponds to the adiabatic ionization potential, and EA represents adiabatic electron affinity.<sup>68</sup> Softness has an inverse relation with twice hardness. There is a counterrelationship between softness and hardness values. The value of "S" should be larger, and the " $\eta$ " value should be lower, increasing the electron acceptance ability for an incredibly effective charge transfer in an OSC. Our proposed molecules follow this trend except for W7. In W1–W6 molecules, the value of softness has risen, leading to greater polarizability and higher delocalization. In contrast, the

hardness value has lessened compared to RW, representing a better charge transfer property.

**3.4. Natural Transition Orbitals.** The use of molecular orbitals naturally describes low-lying electronic transitions in conjugated materials. Natural transition orbitals can be used to analyze compact orbital descriptions for the transition density matrix. It also determines the qualitative information and the nature of the electronic transitions as an alternate method. It is a straightforward approach to simplify the descriptions of mixed overlapping of electronic systems, which are frequently complex in FMO analysis.<sup>69,70</sup> It is used to represent the transitions of the excited state into single hole-particle excitations, and these excitations are represented by a single pair of unoccupied and occupied orbitals.<sup>71</sup>

Based on the TD-DFT results, natural transition orbital analysis (NTO) was executed to provide a compact orbital representation for the electronic transitions and give information about the extent of correlation and extent (percentage) calculated by Multiwfn 3.8.<sup>72</sup> NTO for the first excited state is analyzed to produce the absorption spectra from the optimized ground-state shape.<sup>73</sup> Transitions between the hole and particle are demonstrated in Figure 6.

Excitations have distinct partial charge transfer aspects; the hole density of NTO is located on the donor component of the molecule, and the electron density (particle) of NTO is located on the terminal end.<sup>74</sup> These molecules (W1–W7) have intense transition dipole moments due to the substantial spatial overlap of the hole and electron. RW represents the transition percentage character between hole and particle as 96.53%, and all designed molecules show a transition comparable with RW, such as 93.15, 92.15, 96.44, 96.30, 96.37, 96.25, and 96.83%, as shown in Figure 6, and percentages of transition characters are listed in Table 6.

**3.5. Density of State Estimation.** The density of states assessment elaborates on the range of participation of different parts of the molecules in HOMO and LUMO development. This study is performed to verify the results of the FMO evaluation. It also elaborates on the percentage of Mullikan's charge spreading on each part of the molecule.<sup>75</sup> Similarly, unoccupied and occupied molecular orbital energies of each fragment of W1–W7 molecules are determined by the DOS calculation. For thorough evaluation, according to each molecule's function, it is divided into three regions: the core acceptor area ( $A_1$ ), the donor subunit (D), and the end-group acceptors ( $A_2$ ). This division elaborates on the participation of each part in contributing energy levels of HOMO and LUMO in the percentage form. DOS evaluation was performed utilizing the MPW1PW91 functional at the basis set 6-31G(d,p) of DFT.<sup>76</sup> The analysis of Mullikan's charge density distribution was performed using PyMolyze 1.1 software, and the concluded results are shown in Table 5.

In the DOS graphs (Figure 7), the relative intensity is shown on the y-axis on the left side of the plots. The energies of the orbitals are represented on the x-axis of the DOS plots. The bottom x-axis is divided into three regions: the right side of the portion is considered LUMO, the central planar part represents the band gap between HOMO and LUMO energy levels, and the left side of the portion is considered the HOMO region.<sup>77</sup> Moreover, different colored lines represent the extent of involvement of different moieties in the molecules. In comparison, the role of the terminal acceptors ( $A_2$ ) is represented by the black line, the donor region (D) is represented with red color, the central acceptor ( $A_1$ ) is

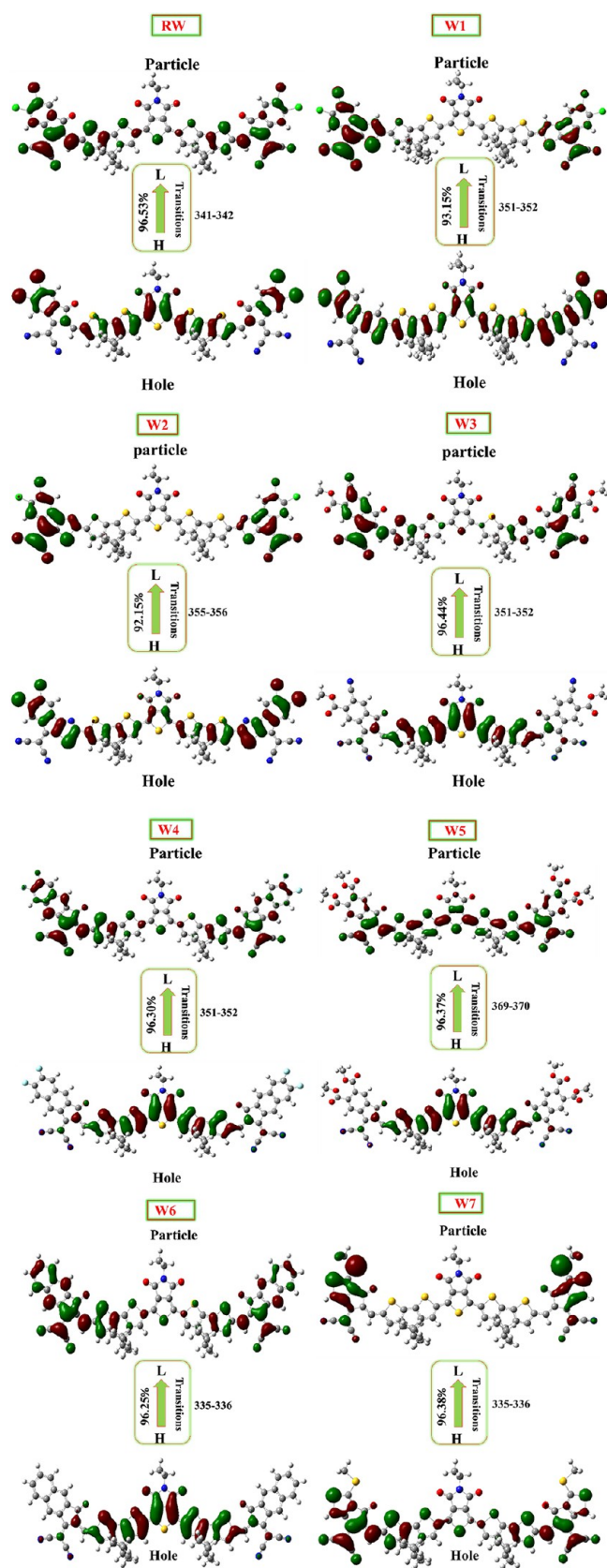


Figure 6. Natural transition orbitals of RW and W1–W7 molecules.

represented with the green line, and the total contribution of all the regions is represented with the blue line. The peaks of all the molecules are different from the other molecules,

Table 5. Percentage Participation of  $A_2$ , Donor, and  $A_1$  in the Rise of HOMO and LUMO

molecules	excitation energy state	percentage contribution of acceptor 2	percentage contribution of donor	percentage contribution of acceptor 1
RW	HOMO	22.1	58.9	19.0
	LUMO	48.2	39.2	12.6
W1	HOMO	21.9	60.0	18.1
	LUMO	80.0	15.6	4.0
W2	HOMO	21.2	60.2	18.7
	LUMO	79.7	16.2	4.1
W3	HOMO	22.8	58.2	19.0
	LUMO	51.7	36.9	11.3
W4	HOMO	23.2	58.3	18.5
	LUMO	49.2	38.3	12.5
W5	HOMO	22.2	58.9	18.9
	LUMO	49.7	38.0	12.3
W6	HOMO	23.1	58.5	18.4
	LUMO	48.3	38.8	13.0
W7	HOMO	23.7	58.1	18.2
	LUMO	47.0	39.6	13.4

signifying the potential of each acceptor moiety to withdraw electrons toward itself.

The results in Table 5 represent that the donor part of the RW molecule has 58.9% participation in rising HOMO while having a 39.2% contribution to rising LUMO energy levels. However, the contribution of  $A_1$  and  $A_2$  acceptors is 19 and 22.1% in HOMO, but central and terminal acceptors' participation in raising the LUMO energy level is up to 12.6 and 48.2%. These facts elaborate that the donor region of the molecule is markedly involved in acting as HOMO, but acceptor parts of the molecules are majorly working at LUMO energy levels. The role of HOMO acting as a donor and LUMO as an acceptor will lead to efficient charge transport from donor to acceptor regions and enhanced charge mobility in the molecule. The donor and acceptor of all of the scrutinized molecules majorly participate in developing the HOMO and LUMO energy levels of the molecules. The donor region has a higher involvement in raising the HOMO energy level. However, in contrast, the acceptor region has a higher contribution to the LUMO energy level.

It can be observed that W1 and W2 have a significantly higher contribution from the donor to the HOMO. It means that HOMO charge density is majorly residing over the donor portion of these molecules, and their terminal acceptors are more capable of acting as LUMO. In molecules other than W1 and W2, LUMO is majorly contributed by terminal acceptors, i.e., acceptor 2. Terminal acceptors in W1 and W2 are robust electron-withdrawing and have a greater potential to attract electrons from central regions. So, due to the presence of these robust electron-withdrawing moieties, the donor portion is less likely to act as LUMO. This phenomenon can be observed in Figure 5, where it can be seen that LUMO charge density is more prevalent across terminal acceptors in W1 and W2 than in other molecules. W1 and W2 perform even better than terminal acceptors having four fluorine atoms, as in the W4 molecule. The reason can be the direct attachment of terminal acceptors with the donor portion, which facilitates the smooth charge transfer from donor to acceptor regions in these molecules.

For excellent charge transportation, the acceptors must substantially contribute to developing the molecules' LUMO.

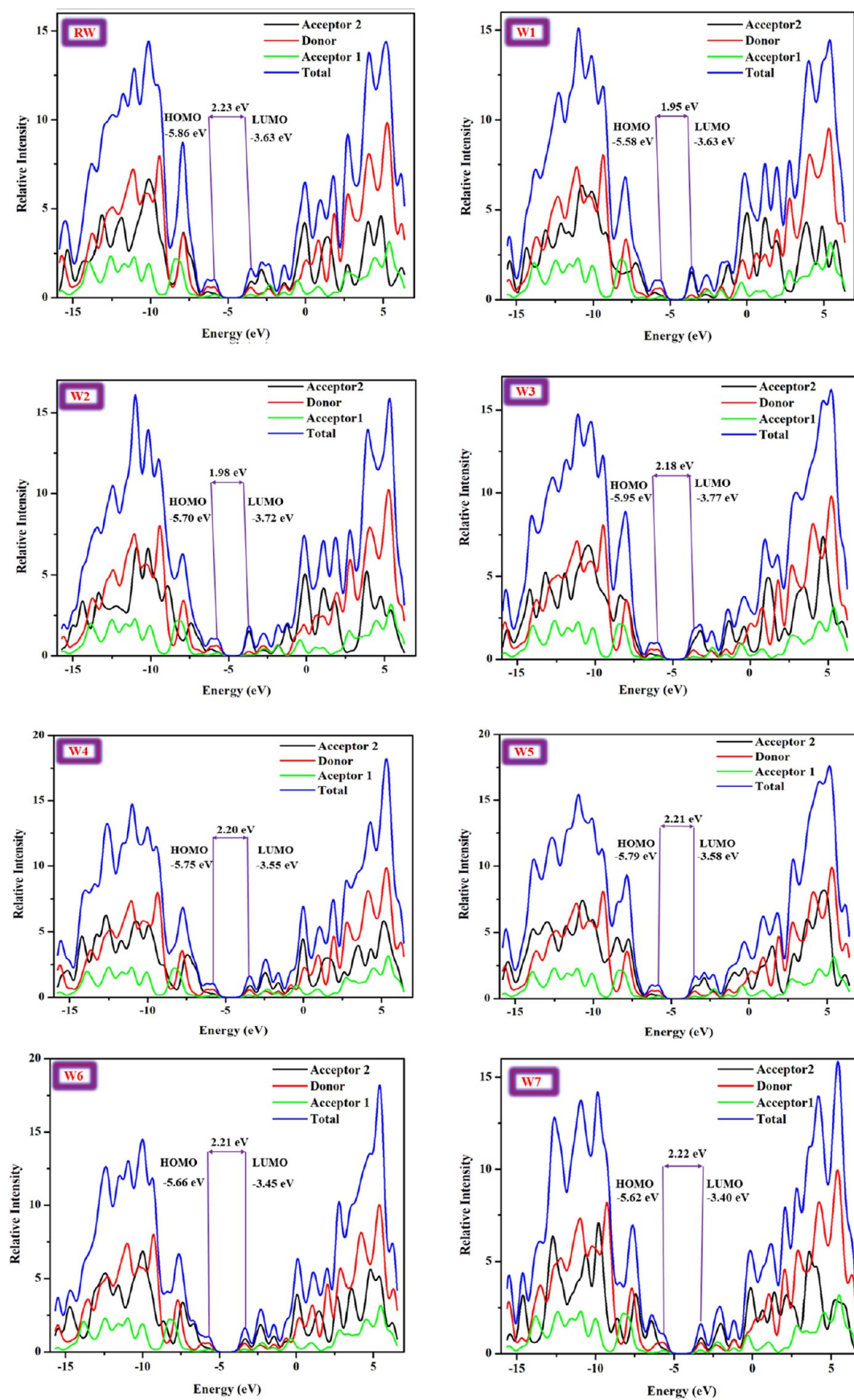


Figure 7. DOS maps of RW and W1–W7.

All perceived molecules (W1–W7) have significant contributions in developing LUMO energy levels; these molecules exhibit efficient charge transfer abilities due to electron-withdrawing moieties at the peripheral positions.<sup>78</sup> It can be viewed that the W1 molecule has a significant contribution to the development of the LUMO region. The percentage increase in the LUMO value of W1 (80%) compared to RW (48.2%) is due to the robust electron-withdrawing capability of the terminal acceptor (A<sub>2</sub>). The percentage value of LUMO has increased in the W1–W5 molecule, which indicates that terminal acceptors of these designed molecules have a better withdrawing capability than RW. Therefore, these molecules are a good choice for synthesizing advanced organic solar cells.

**3.6. Analysis of Reduced Density Gradient.** The nature of weak interactions is determined using the noncovalent interaction index, which is used to characterize intermolecular interactions. Based on a reduced density gradient (RDG), the noncovalent interaction method represents weak spatial interaction and gives information about the interactions between host and guest in a complex.<sup>79</sup> The regions of the molecules that experience intermolecular and intramolecular noncovalent interactions are graphically visualized using the RDG analysis.<sup>80</sup> It is a nondimensional quantity. We can comprehend the type and strength of molecular interaction by inspecting the electron density amount of the RDG versus  $\text{sign}(\lambda_2)\rho$  peaks.<sup>81</sup> Repulsion (nonbonded) and attraction (bonded) interaction can be denoted as the  $\lambda_2 > 0$  and  $\lambda_2 < 0$  signs. These interactions are visualized by VMD and Multiwfn software. Van der Waals interactions ( $\lambda_2 \approx 0$ ) present between the hydrogen atom are shown by green, repulsive interactions (steric effect) present within the ring are shown by dotted red, and hydrogen bonding interactions are represented by blue in Figure 8. The larger negative values of  $\text{sign} \lambda_2$  represent the stronger attractive interactions in our molecules; this shows strong hydrogen bonding, and low steric repulsion leads to greater stabilization in our molecules. It is measured by eq 8.<sup>82</sup>

$$\text{RDG}(r) = \frac{1}{2(3\pi^2)^{1/3}} \frac{|\nabla\rho(r)|}{\rho(r)^{4/3}} \quad (8)$$

Small red patches can be seen on the isosurface analysis of our designed molecules (W1–W7), representing that intramolecular steric repulsions rather than intermolecular repulsions are attributed to more prominent energy exchange. van der Waals interactions are evident in vast numbers of green patches in our molecule (W1–W7).

**3.7. Optical Property Analysis.** The optical boundaries of molecules play a vital role in the photovoltaic properties of the OSCs. Discrete optical parameters of all molecules were computed and investigated computationally, such as each molecule's oscillator strength, absorption properties, and excitation energies.<sup>83,84</sup> An absorption spectrum is very effective in elaborating the optoelectronic properties of the molecules. Chromophore absorbs only that part of radiation whose energy matches the band gaps and enters an excited state. A chromophore with a low excitation energy, a broader absorption profile, and high oscillator strength enhances absorption at a higher molar absorption coefficient ( $\epsilon$ ). It is expected to produce prominent intramolecular charge transfer (ICT), representing its efficient performance in organic solar cells.<sup>85</sup> The examined optical properties of RW and W1–W7

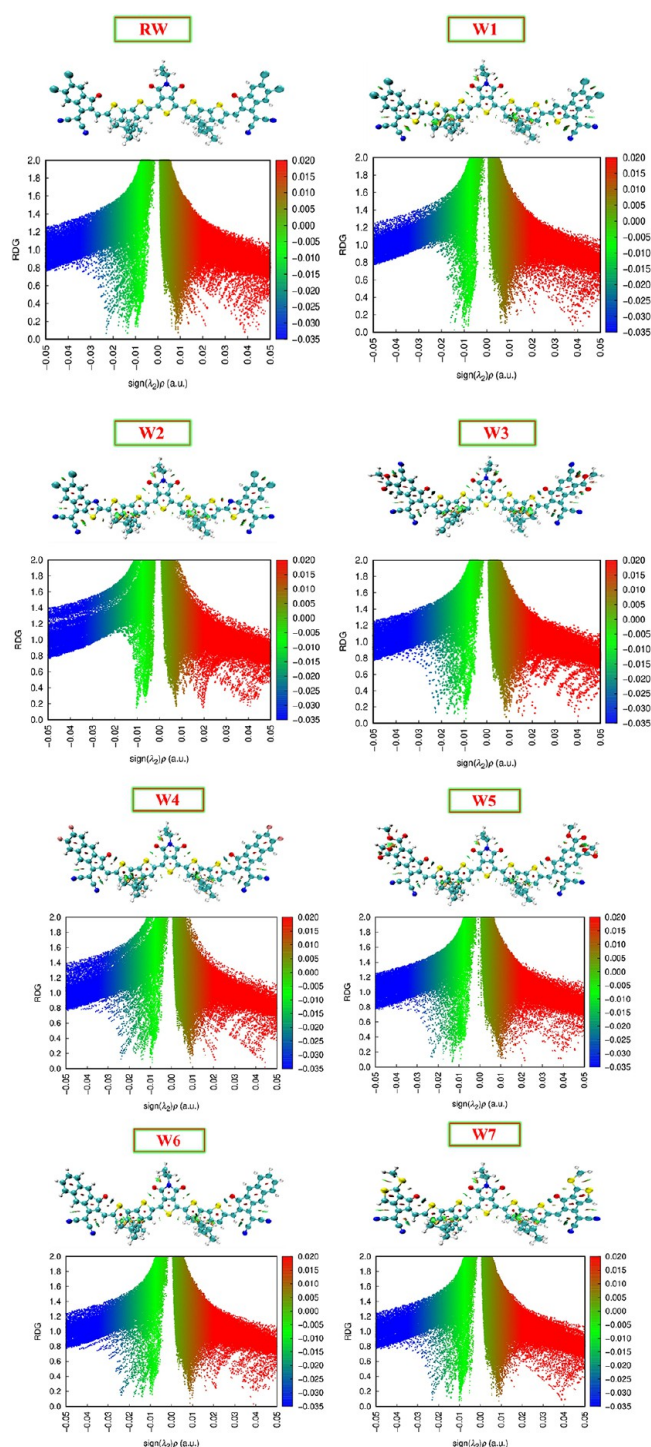


**Figure 8.** NCI and RDG representation of RW and W1–W7 molecules.

in solvent and the gaseous medium are tabulated in Tables 6 and 7, respectively.

Figure 9 depicts the absorption maximum of all molecules in the gas and solvent phase. All newly conceived molecules except W7 represent enhanced  $\lambda_{\text{max}}$  compared to the RW molecule in the gaseous phase. W7 has  $\lambda_{\text{max}}$  values comparable to the RW molecule. The RW represents  $\lambda_{\text{max}}$  up to 673 nm; however, all the scrutinized molecules from W1–W7 show  $\lambda_{\text{max}}$  as 768, 760, 684, 681, 675, 677, and 672 nm, respectively, in the first excited state. The increasing order of  $\lambda_{\text{max}}$  of all

**Table 6. Excitation Energy ( $E_x$ ),  $\lambda_{\max}$ , Oscillator Strength ( $f$ ), and Transition Percentage of NTOs of RW and W1–W7 Without Solvent**

molecules	calculated $\lambda_{\max}$ (nm)	excitation energies $E_x$ (eV)	oscillator strength ( $f$ )	transition character (%)
RW	673	1.84	3.17	96.53%
W1	768	1.61	2.10	93.15%
W2	760	1.63	2.01	92.11%
W3	684	1.81	3.14	96.44%
W4	681	1.81	3.32	96.30%
W5	675	1.83	3.16	96.37%
W6	677	1.83	3.31	96.25%
W7	672	1.84	3.08	96.38%

**Table 7. Excitation Energy ( $E_x$ ),  $\lambda_{\max}$ , Oscillator Strength ( $f$ ), and Reaction Energy of RW and W1–W7 in solvent Chloroform**

molecules	exp. $\lambda_{\max}$ (nm)	calculated $\lambda_{\max}$ (nm)	excitation energies $E_x$ (eV)	oscillator strength ( $f$ )
RW	728	719	1.72	3.43
W1		839	1.47	2.36
W2		833	1.48	2.20
W3		736	1.68	3.33
W4		725	1.70	3.60
W5		722	1.71	3.36
W6		720	1.72	3.60
W7		715	1.73	3.39

molecules is  $W7 < W5 < W6 < W4 < W3 < W2 < W1$ . All these devised molecules represent absorption in the visible region. The **W1** molecule represents broader absorption due to the presence of four Cl atoms (exhibiting a strong electron-withdrawing effect) in the terminal acceptor ( $A_2$ ) region. The presence of these electron-withdrawing atoms along with the  $-CN$  group resulted in the reduction in the band gap that leads toward a higher absorption wavelength in this molecule. **W2** also represents efficient absorption up to 760 nm in the gaseous phase due to the presence of the thiazole ring in the  $A_2$  acceptor of this molecule.

In chloroform solvent, the  $\lambda_{\max}$  of **RW** is 719 nm. However, from all perceived molecules, **W1–W7** represent higher absorption in chloroform solvent than that of the **RW** molecule. The range of  $\lambda_{\max}$  in all of the perceived molecules is 715–839 nm. **W1** and **W2** molecules show the highest  $\lambda_{\max}$  in the solvent phase and exhibit the red-shift phenomenon in chloroform in the near IR region. Furthermore, **W1** and **W2** also show strong shoulder peaks in the solvent medium. It can be due to the presence of higher-energy excitonic states along with the complex electronic structure of molecules, including various conjugated segments. On the other hand, **W3–W7** show a single broad absorption peak that can be due to their structural variation as compared to **W1** and **W2**. **W3–W7** contain a bridged carbon atom present between the core and terminal acceptor, which is involved in increasing the conjugation, which leads to an enhanced delocalized  $\pi$ -electron system in these molecules. The increasing order of  $\lambda_{\max}$  absorption of molecules is  $W7 < RW < W6 < W5 < W4 < W3 < W2 < W1$ . However, the spectra of all of the devised molecules show that **W1** and **W2** show significantly longer absorption wavelengths than **RW**. Furthermore, except for the **W7** molecule, other molecules also show slightly longer absorption wavelengths due to the presence of  $\pi - \pi^*$

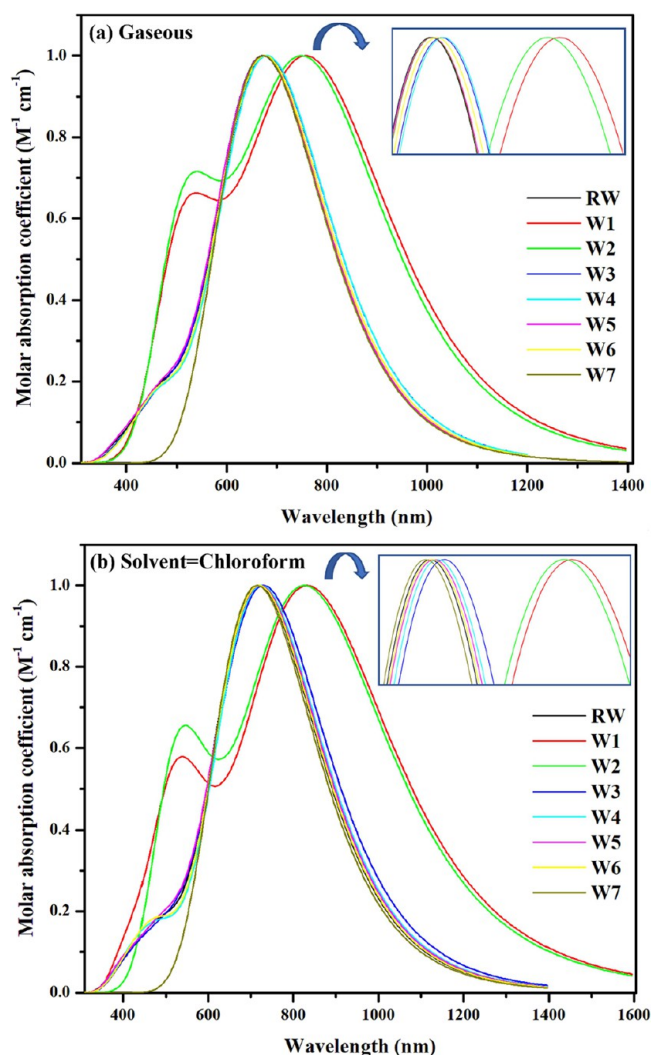


**Figure 9.** (a) Absorption spectra of RW and W–W7 in the gas phase. (b) Absorption spectra of RW and W1–W7 in a chloroform solvent.

electronic transitions and strong electron-withdrawing moieties in the terminal acceptors.

Individually, between the **W3** and **W4** molecules, **W3** has more excellent absorption than **W4** because of the presence of two cyanide groups and two methoxide groups on terminal acceptors and has a robust withdrawing ability that causes the redshift of  $\lambda_{\max}$ . Furthermore, **W4** has a better  $\lambda_{\max}$  value than **W5** because four electronegative fluorine atoms on the terminal acceptor cause greater  $\lambda_{\max}$  due to the high electron-withdrawing capability.

The amount of minimal energy required for the electronic transfer from the ground to the excited state is the excitation energy ( $E_x$ ).<sup>86</sup> If a molecule's band gap is large, the value of  $E_x$  will be more significant.  $E_x$  value should be lower for efficient absorption and electronic transition. In our research work, **W1–W7** molecules have lower  $E_x$  values than **RW**, which shows that our designed molecules have greater charge mobility and absorption due to their strong withdrawing groups on terminal acceptors that pull the electrons toward themselves and cause the reduction in the band gap.

Oscillator strength " $f$ " and  $E_g$  have a linear relationship. Oscillator strength is directly related to the light harvesting efficiency. These are calculated from the first excitation state of

our molecules.<sup>87</sup> Our proposed molecules **W4** and **W6** have greater oscillator strength values than **RW** in the solvent and gaseous phases, indicating that these molecules have greater efficiency and a remarkable ability to exploit the absorbed radiation. This behavior tends to provide better sites for intermolecular charge transfer and show more incredible electronic transitions. According to the results of  $\lambda_{\max}$ ,  $E_x$ , and  $f_j$ , among all the proposed molecules, **W1** has greater  $\lambda_{\max}$  and least excitation energy than **RW**, showing that terminal acceptors of these molecules seem to be more efficient than **RW**.

**3.8. Dipole Moment.** The dipole moment is vital in determining the orderliness, charge accommodation, charge separation, and solubility of the designed molecules in organic solvents.<sup>88</sup> The dipole moment of **RW** and **W1–W7** molecules was calculated in both gaseous and solvent phases utilizing our aforementioned MPW1PW91 functional. The higher value of the dipole moment enhances the molecule's ability to possess more electrons and self-assembly of molecules. The molecules with greater dipole moment values also play a crucial role in manufacturing elegant OSC solutions. Therefore, solubility in organic solvents is based on the dipole moment of organic molecules. Longer supramolecular chains are induced by good self-assembly of molecules due to more prominent dipole moments, which can facilitate the infiltration pathways of holes and electrons and increase the level of coordination at the donor–acceptor junction.

Moreover, enhanced smoothness obtained by a more significant dipole moment leads to higher charge transmission and shows greater polarity in polar solvents.<sup>89</sup> The results of the dipole moment obtained in both the solvent and the gaseous medium are represented in Table 8. Table 8 shows

**Table 8. Dipole Moment in Solvent Chloroform  $\mu_s$  and Without Solvent  $\mu_g$**

molecules	dipole moment $\mu_g$	dipole moment $\mu_s$
<b>RW</b>	0.629551	1.755074
<b>W1</b>	3.344320	4.039433
<b>W2</b>	0.656457	1.625549
<b>W3</b>	3.178173	4.906712
<b>W4</b>	1.586171	1.240767
<b>W5</b>	5.105051	4.900269
<b>W6</b>	5.285189	5.471581
<b>W7</b>	6.078760	6.249860

that in the gaseous and solvent (chloroform) medium, **W7** represents the maximum value of the dipole moment. Because of the emergence of the dipole–dipole interaction, higher dipole moments are advantageous for hole transport, reducing charge recombination, and improving FF. The increasing trend of dipole moment in the gaseous medium is **RW** < **W2** < **W4** < **W3** < **W1** < **W5** < **W6** < **W7**.

In the solvent medium, the increasing order of the dipole moment is **W4** < **W2** < **RW** < **W1** < **W5** < **W3** < **W6** < **W7**. Comparing the dipole moment values of scrutinized molecules with the reference molecules, **W2** and **W4** represent a decrease in the dipole moment values in a solution medium. This may happen due to an extension of a conjugated network at the ends of acceptor 2. **W7** represents the highest dipole moment values in both phases. **W7** contains huge-sized sulfur atoms, which are responsible for the greater spatial separation of charge, leading to increased intramolecular charge transfer and

maximum charge separation toward terminal acceptors. Moreover, **W7** contains polar  $-S-CH_3$  groups, which can also enhance the polarity of this molecule. It shows that the **W7** molecule is the most suitable candidate for the manufacturing of solution-processable OSC devices.

**3.9. Molecular Electrostatic Potential and Mulliken Charge Distribution.** MEP and MCD evaluation provides fruitful information on intramolecular charge transfer on the molecules' electropositive and electronegative parts. The maps of MEP and MCD specify the electrophilic and nucleophilic areas of the molecules that are appropriate sites for hydrogen bonding. It elaborates electronic clouds on the different regions of the 3D shape molecule highlighted with different colors.<sup>90,91</sup> Therefore, estimating the possibility of electrophilic and nucleophilic attacks on different molecular areas is convenient. In the MEP figures, red exhibits the highly electronegative regions, yellow represents reasonable electronegative regions, and blue displays the electropositive parts. The more significant distance between blue and red means the ease of charge separation.<sup>92</sup> The MEP maps of **RW** and all of the conceived molecules **W1–W7** are represented in Figure 10.

The MEP map elaborates that there is an appropriate gap between the blue and red colors, which heightens the efficient electronic distribution within the molecule based on the electronegativity of each moiety. The end group acceptor (**A<sub>2</sub>**) of every molecule has a red color on the nitrogen atoms of the  $-CN$  groups, which elaborates the negative potential present in that region, i.e., the nucleophilic area. The central part of each molecule has a blue color that represents the positive potential present in the molecules, i.e., the electrophilic part. All molecules with greater separation of the electronegative and electropositive regions represent the stability of those molecules.

**3.10. Transition Density Matrix Evaluation.** TDM plots elaborate on the electronic transitions around different molecular regions in a first excited state and provide an understanding of the localization of electrons and holes. Charge transportation may be viewed off-diagonal and diagonally in the excited state in concerned plots. TDM plots specify the charge density by different colors, ranging from dark blue at the end (zero electron density) to bright red at another extreme (high charge density) of the concerned molecule. The effect of all hydrogen atoms is not considered due to their small role in the transition of electrons.<sup>93</sup> The studied molecules are divided into different parts according to the role and nature of every moiety present in that molecule. The moieties were labeled as terminal acceptors (**A<sub>2</sub>**), the donor part (labeled as **D**), and central acceptors (**A<sub>1</sub>**). In TDM graphs, the right y-axis displays electron density in various colors, while the left y-axis and bottom x-axis represent the molecules' heavy atoms.

It can be seen that some extent of uniformity exists in the charge transport of all of the conceived molecules. In TDM plots (Figure 11), brighter regions represent the occurrence of charge transfer from the donor toward the terminal end groups. It is evident that a more illuminated portion is present in the **D** and **A<sub>2</sub>** parts of the molecule; however, a portion of these fringes is also present in the **A<sub>1</sub>** part of the molecule. The brightest fringes in the **A<sub>2</sub>** region of **W1** and **W2** represent the high electron density and greater ease of electronic transitions in these molecules. It is analyzed from the TDM maps that these two molecules have a small dark blue zone, which is

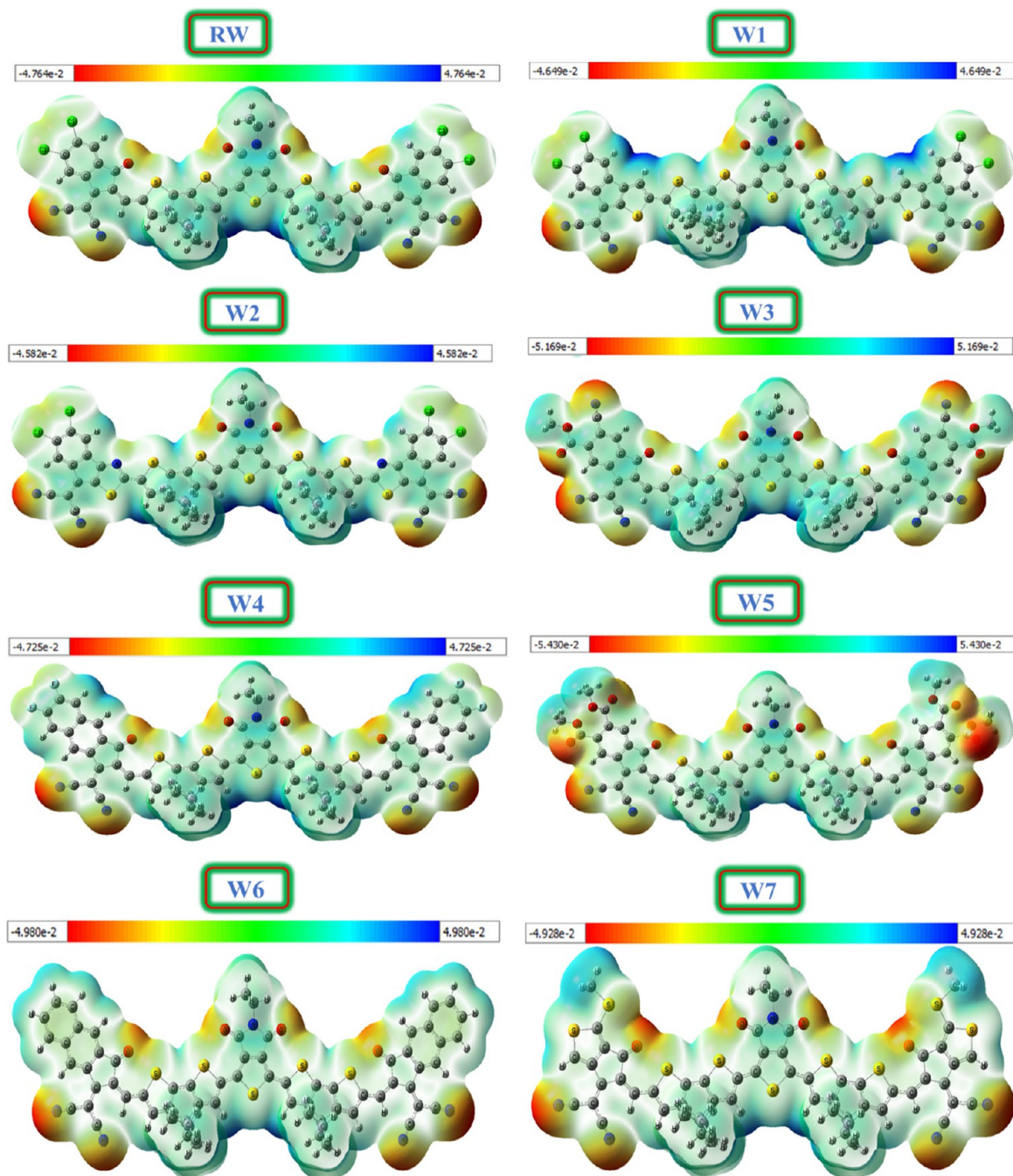


Figure 10. Represent the MEP maps of RW and W1–W7.

fruitful for the movement of charges within the molecular structure. Due to the properties, such as (1) scattering of charges, (2) lower energies of excitations, and (3) higher chromophore absorption, W1 and W2 can be declared as the best molecules in the devised series.

**3.11. Binding Energy and Interaction Coefficient.** The lowest energy required for splitting exciton into its constituents (electron and hole) is known as the binding energy; this splitting occurs at the excited state resulting from photoexcitation.<sup>94</sup> Exciton binding energy is vital in analyzing OSCs' exciton potential, dissociation, and photovoltaic properties. It has an inverse relation with the splitting of electrons, such as less binding energy values, leading toward more exciton dissociation, which resultantly assists in transporting charges

toward concerned electrodes. However, this energy directly relates to Coulombic forces between the electrons and holes. The ability of the terminal and central acceptors to attract electrons also facilitates electron–hole pair separation.<sup>95</sup> The Coulombic forces of attraction are neutralized by lower binding energy values and strong electron acceptor groups that enable easier exciton splitting. Binding energy values can be obtained by utilizing the below eq 9.

$$E_b = E_g - E_x \quad (9)$$

where  $E_g$  shows the band gap and  $E_x$  represents excitation energy values. Computationally concluded binding energy values in both gaseous and a solvent medium of reference and designed molecules are listed in Table 9.

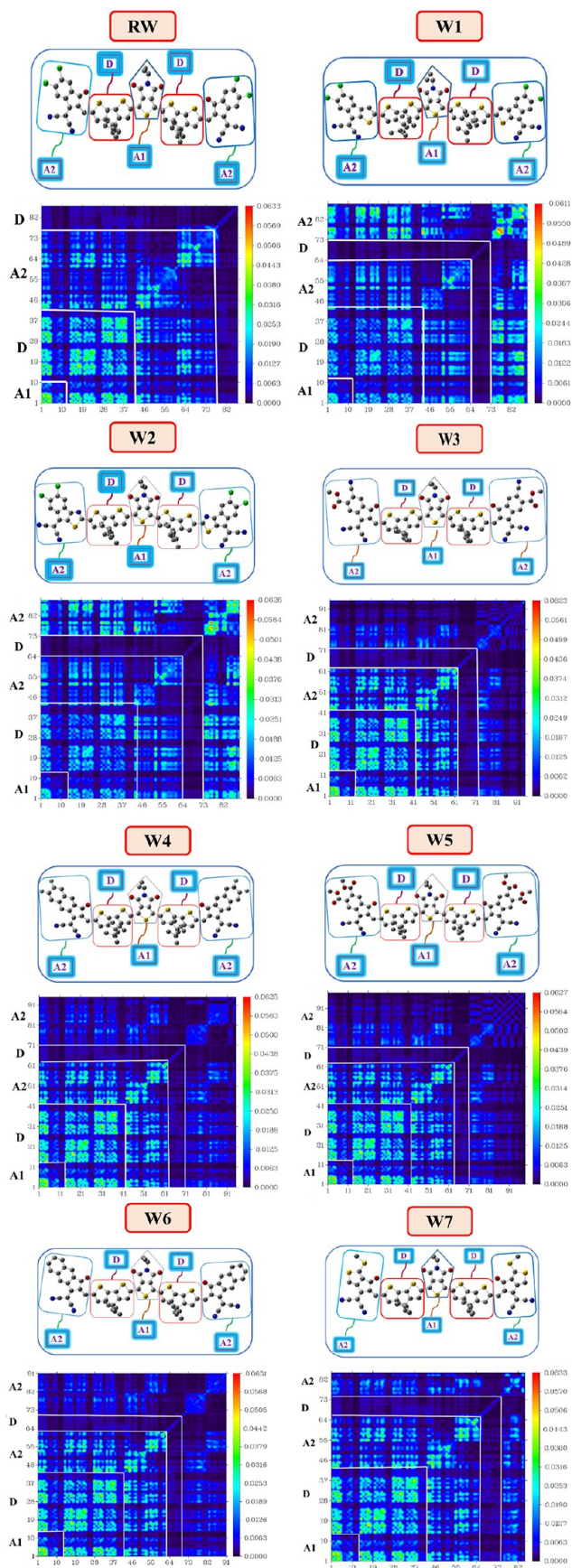


Figure 11. TDM Maps of RW and W1–W7.

Table 9.  $E_b$  Values and Interaction Coefficients of Molecules in the Gaseous and Solvent Phases

molecules	$E_b$ (eV) gaseous	$E_b$ (eV) solvent	interaction coefficient (g)	interaction coefficient (s)
RW	0.39	0.51	0.69473	0.68892
W1	0.34	0.48	0.68248	0.67831
W2	0.35	0.49	0.67865	0.67581
W3	0.37	0.49	0.69441	0.68739
W4	0.38	0.49	0.69454	0.68870
W5	0.37	0.49	0.69417	0.68788
W6	0.38	0.49	0.69375	0.68853
W7	0.38	0.49	0.69419	0.68898

In the gaseous phase, RW represents a binding energy of 0.39 eV. All the devised molecules exhibit nearly similar binding energy values within the 0.34 to 0.39 eV range. W1 represents the most negligible  $E_b$  value among all of the newly designed molecules. In the solvent phase (chloroform solvent), the binding energy ( $E_b$ ) values of RW and all the scrutinized chromophores (W1–W7) are 0.51, 0.48, 0.49, 0.49, 0.49, 0.49, 0.49, and 0.49 eV, respectively. All the studied molecules have lower binding energy values than RW. The W1 molecule has the lowest  $E_b$  value due to excellent terminal acceptor ( $A_2$ ) moieties on both ends of the molecules, which pull electrons toward themselves by surpassing the Coulombic forces between the atoms. However, all these devised molecules have prominent charge separation abilities. Therefore, these perceived molecules can be utilized as efficient OSCs.

The interaction coefficient is an essential factor for evaluating the efficiency of OSCs because it affects the movement of the charges within a molecule. The lower interaction coefficient values enhance the charge mobility of the molecule. This shows that charge movement across the molecule is efficient due to the low interaction coefficient.<sup>96</sup> The interaction coefficient value of RW in the solvent phase is 0.68892. However, scrutinized molecules W1–W7 represent interaction coefficient values of 0.67831, 0.67581, 0.68739, 0.68870, 0.68788, 0.68853, and 0.68898, respectively. All molecules have lower interaction coefficient values in the gaseous phase than RW, indicating efficient movement of charges from the core part to the end groups. Similarly, all molecules except W7 have a lower interaction coefficient in the solvent phase than RW. W1 and W2 molecules represent the least interaction coefficient values. Therefore, these scrutinized molecules exhibit better charge transfer properties, enabling them to be used as OSCs.

**3.12. Light Harvesting Efficiency Analysis.** LHE is an efficient tool for evaluating a material's ability to produce charge carriers using light energy. LHE is mainly concerned with charge production, and its analysis is very beneficial in elaborating the performance of our studied molecules. Moreover, it helps estimate the power conversion efficiency of organic solar cells.<sup>97</sup> The LHE has a direct relation with  $J_{sc}$ . The high value of the LHE corresponds to a high  $J_{sc}$  value and eventually leads toward a high PCE of the molecule. The LHE of the OSC molecules is calculated by utilizing eq 10.

$$\text{LHE} = 1 - 10^{-f} \quad (10)$$

Here, " $f$ " represents the oscillator strength of the molecules in the solvent phase. The examined LHE values of all of the scrutinized molecules are tabulated in Table 10. It can be

**Table 10.** Oscillator strength “*f*” and LHE of RW and W1–W7

molecules	oscillator strength ( <i>f</i> )	LHE (eV)
RW	3.43	0.9996
W1	2.36	0.9956
W2	2.20	0.9936
W3	3.33	0.9995
W4	3.60	0.9997
W5	3.36	0.9995
W6	3.60	0.9997
W7	3.39	0.9995

visualized from the tabulated data that W4 and W6 exhibit the highest LHE value of 0.9997 eV. The increasing LHE trend of the perceived chromophores is as follows: W2 < W1 < W3 = W5 = W7 < RW < W4 = W6. This order reveals that W4 and W6 molecules exhibit enhanced LHE values than the RW molecule. Moreover, it can be noticed that W1 and W2 have LHE values lower than RW due to their low oscillator strength. These data reveal that W4 and W6 can have a better potential to harvest sunlight energy. Due to improved LHE, these molecules have the potential to produce high  $J_{sc}$ , which is vital to boost the PCE of solar cells. Therefore, these molecules might be considered to be a good selection for producing promising OSCs in the future.

**3.13. Internal Reorganization Energy Analysis.** The reorganization energy is utilized to study the link between the molecular structure and the participation of compounds in charge transportation, which helps in designing the most efficient moieties for solar cell applications. There is an inverse relation between the charge transfer ability and the reorganization energy of a molecule. So, a molecule with efficient charge mobility also has a low reorganization energy value.<sup>98,99</sup> In this research, external reorganization energy is neglected due to its dependence on external factors such as polarization, which has a trivial effect. However, internal RE depends on the abrupt variations occurring in the intrinsic structure of organic molecules. Internal RE is used to evaluate the charge transfer performance of a molecule. The internal energy of an electron is symbolized by ( $\lambda_e$ ), and the internal energy of a hole is denoted by ( $\lambda_h$ ). The internal energy ( $\lambda_{int}$ ) values were asserted by eqs 1 and 2, and asserted values are summarized in Table 11.

The RW molecule represents the 0.006898 eV value for  $\lambda_e$ ; however, all proposed molecules W1–W7 exhibit  $\lambda_e$  of 0.004686, 0.0045588, 0.0061544, 0.0065729, 0.0069477, 0.0066182, and 0.0071881 eV, respectively. W1 and W2 molecules exhibit the least  $\lambda_e$  values that represent the efficient charge mobility of these molecules due to extended

**Table 11.** Represents the  $\lambda_e$  and  $\lambda_h$  Values of RW and W1–W7 Molecules

molecules	$\lambda_e$ (electron)	$\lambda_h$ (hole)
RW	0.006898	0.0080152
W1	0.004686	0.0086021
W2	0.0045588	0.0079072
W3	0.0061544	0.0080396
W4	0.0065729	0.0040511
W5	0.0069477	0.0082234
W6	0.0066182	0.0076701
W7	0.0071881	0.0075951

conjugation present in the terminal acceptors ( $A_2$ ) of these molecules. The  $\lambda_h$  value of the RW molecule is 0.0080152 eV, while for newly perceived molecules, the RE values of the hole are 0.0086021, 0.0079072, 0.0080396, 0.0040511, 0.0082234, 0.0076701, and 0.007551 eV. The  $\lambda_h$  of all studied molecules has an increasing order as W4 < W7 < W6 < W2 < RW < W3 < W5 < W1. The  $\lambda_e$  of all scrutinized molecules exhibits increasing order as W2 < W1 < W3 < W4 < W6 < RW < W5 < W7. It can be analyzed from the  $\lambda_e$  trend that W1, W2, W3, W4, and W6 molecules represent efficient results for charge movements due to substituting terminal acceptors of RW molecules.

**3.14. Open Circuit Voltage.** When the current passing through the circuit is zero, the highest voltage value in a circuit is known as the open circuit voltage. It mainly affects the PCE of organic solar devices because it is directly proportional to PCE. Moreover, the  $V_{oc}$  of a molecule must be high because it leads to the generation of efficient OSCs, specifically more than 1 V.  $V_{oc}$  is analogous to the energy difference between the HOMO of the donor and LUMO of the acceptor materials correspondingly. Other parameters like light intensity, source of the light, temperature, and charge transportation also impact the  $V_{oc}$  value. Scharber and colleagues developed a simple formula to calculate the  $V_{oc}$  of solar cells.

$$V_{OC} = \frac{1}{e}(E_{HOMOofdonor} - E_{LUMOofacceptor}) - 0.3 \quad (11)$$

In eq 11, 0.3 is mainly utilized to produce charges at the junctions. It is clear from the abovementioned equation that the band gap between the LUMO of the acceptor and the HOMO of the donor material strongly influences  $V_{oc}$ . Due to its wide usage, we used PTB7 as donor material in this approach. Results obtained by utilizing a standard donor and an acceptor material with the assistance of HOMO and LUMO energy values give us an essential insight into the performance efficiency of molecules. The cited HOMO and LUMO values of PTB7 are −5.15 and −3.31 eV, respectively.<sup>100</sup> Table 12 highlights the computed  $V_{oc}$  values for each of the compounds that were studied.

**Table 12.** Calculated Values of the Open Circuit Voltage  $V_{oc}$  and Normalized  $V_{oc}$  of RW and W1–W7 Molecules

molecules	$V_{oc}$ (eV)	normalized $V_{oc}$
RW	1.22	47.1498
W1	1.22	47.1498
W2	1.13	43.6715
W3	1.09	41.7391
W4	1.30	50.2415
W5	1.27	49.0821
W6	1.40	54.1063
W7	1.45	56.0386

RW shows a  $V_{oc}$  value of 1.22 eV with PTB7 donor; however, scrutinized chromophores (W1–W7) exhibit  $V_{oc}$  values of 1.22, 1.13, 1.09, 1.30, 1.27, 1.40, and 1.45 eV respectively. It is clear from the analyzed data that the W7 molecule exhibits the highest  $V_{oc}$  in comparison to the RW molecule with the PTB7 donor polymer. The increasing order of  $V_{oc}$  of all studied molecules is W3 < W2 < W1 = RW < W5 < W4 < W6 < W7. It can be noticed that W2 and W3 show low values of  $V_{oc}$  as compared to the pre-existing RW molecule. On the other hand, W4–W7 show improved open

circuit voltage values. W7 represents the highest  $V_{oc}$  among the compounds that have been studied, as shown in Figure 12. The

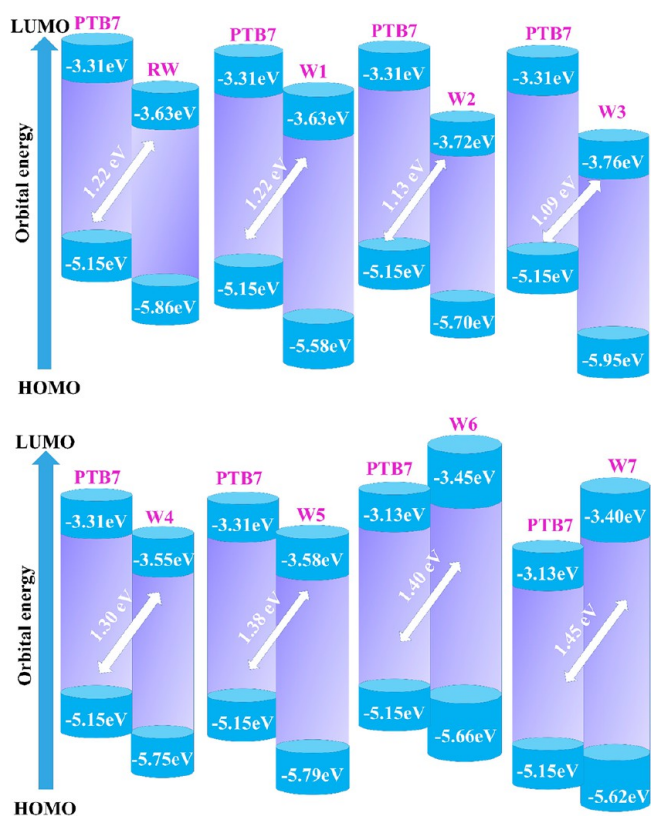


**Figure 12.** Representation of the open circuit voltage ( $V_{oc}$ ) of RW and W1–W7 molecules.

LUMO of the W7 (−3.40 eV) molecule resides on the highest energy point as compared to the LUMOs of all other studied chromophores. The  $V_{oc}$  value of OSCs will increase as the energy difference between the HOMO of donor material and LUMO of acceptor materials increase.

Because of some critical parameters such as  $\lambda_{max}$ , energy gap, excitation energies, light harvesting efficiencies, binding energies, dipole moment, and reorganization energies values, we can estimate the improvement in the efficiency of OSCs. These results indicate that W4 and W6 show better results than RW in computed parameters. The efficacy of newly introduced terminal acceptors in W1–W7 molecules makes them excellent candidates for the next NFAs in OSCs.

**3.15. Charge Transfer Analysis.** For the evaluation of the transition nature and charge transfer (CT) between donor polymer PTB7 and acceptor molecules, blend formation (complex study) is a significant parameter. The optimum charge transfer between the donor and acceptor can sustain a greater power conversion efficiency. The complex is formed by using an appropriate acceptor and PTB7, a donor polymer frequently used for the practical application of organic solar cells. The relative positioning and configuration of acceptor molecules and donor polymer PTB7 facilitates charge transformation between the electron-donating and -accepting components and significantly impacts the electronic cloud of the acceptor molecules and donor polymer PTB7 configuration.<sup>101,102</sup>

As shown in Figure 13, the donor polymer is oriented precisely parallel to acceptor W1 with an ideal distance. The

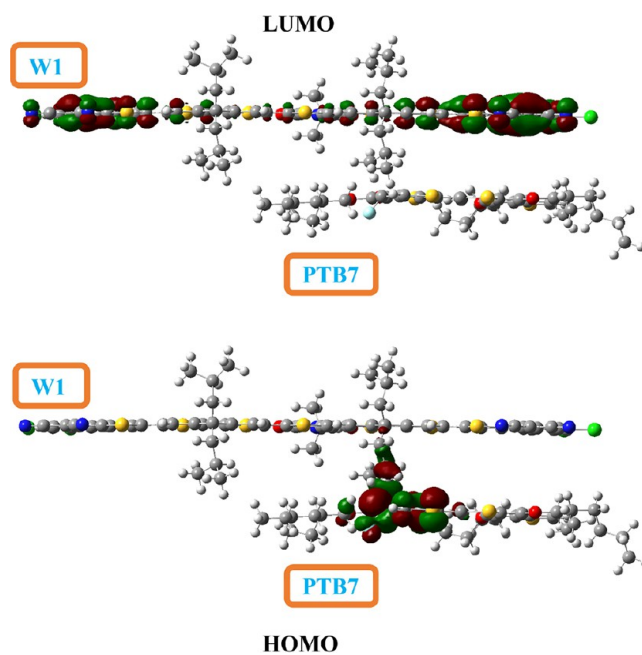


**Figure 13.** Electronic charge distribution of HOMO and LUMO on PTB7 concerning the W1 acceptor W1 molecule.

charge transfer and excitation process must be carried out in this orientation. Planarity plays a crucial role in efficient charge transfer between both molecules because planarity permits molecules to pack more firmly for more excellent crystallinity and leads to greater CT.<sup>103</sup> The W1 acceptor molecule is selected due to its lowest band gap, maximum absorption, less binding energy, and less excitation energy for an efficient charge transfer in a polymer donor–acceptor complex. Charge circulation and electronic structure patterns were calculated at the B3LYP/6-31G(d,p) level of DFT. It can be seen from Figure 13 that HOMO is located on the donor polymer PTB7, and LUMO is located on the end group of acceptor molecule W1. The FMO study of the complex shows that electronic charge transfer occurs from donor polymer PTB7 to the W1 acceptor molecule. It can be concluded that newly proposed molecules are good candidates for the practical application of efficient charge transfer in OSCs.

#### 4. CONCLUSIONS

This research introduced seven novel OSC molecules with efficient terminal acceptors by utilizing the selected MPW1PW91 functional with the 6-31G(d,p) basis set and TD-SCF method used for the solvent phase. The results represented a considerable improvement in all of the scrutinized molecules, making this study very fruitful for practical utilization. Except for W7, all other scrutinized molecules represent a bathochromic shift in the solvent phase ranging from 722 to 839 nm, and the gaseous phase ranges from 675 to 768 nm, respectively, compared to the reference molecule (RW). Moreover, reduced band gap values of all of the perceived molecules compared to RW are immensely fruitful in OSC utilization. W1 molecules exhibit efficient optoelectronic properties, including the lowest band gap of 1.95 eV and the most negligible exciton binding energy value of 0.48 eV in the solvent phase and the highest  $\lambda_{max}$  values in both solvent 839 nm and gaseous 768 nm phases. The W4 molecule represents the highest LHE value of 0.9997 eV. The

W7 molecule exhibits the highest dipole moment value in the solvent and gaseous phases. Almost all proposed molecules W1–W7 have an improvement in charge transfer because they have the lowest value of electron and hole mobility. W2, W4, and W6 have the lowest electron and hole mobility values compared to RW. The W2 molecule has the lowest value of interaction coefficient, representing the better charge transfer characteristic among all molecules. Except for W2 and W3 molecules, all studied molecules represent higher  $V_{oc}$  values calculated according to their HOMO and LUMO values with polymer donor complex PTB7 compared to the RW molecule. All of these results explore successful terminal acceptor modification of C8C8–4Cl in this research.

## AUTHOR INFORMATION

### Corresponding Authors

**Samia Ben Ahmed** – Department of Chemistry, College of Science, King Khalid University, Abha 61421, Saudi Arabia; Email: sbahmad@kku.edu.sa

**Rasheed Ahmad Khera** – Department of Chemistry, University of Agriculture, Faisalabad 38000, Pakistan; [orcid.org/0000-0002-5513-8096](https://orcid.org/0000-0002-5513-8096); Email: rasheedahmadkhera@yahoo.com, rasheed.ahmad.khera@uaf.edu.pk

**Abeer A. Hassan** – Department of Chemistry, College of Science, King Khalid University, Abha 61421, Saudi Arabia; Department of chemistry, Faculty of science for Girls, Ain Shams University, Cairo 11566, Egypt; Email: aalli@kku.edu.sa

### Authors

**Tanzeela Noor** – Department of Chemistry, University of Agriculture, Faisalabad 38000, Pakistan

**Muhammad Waqas** – Department of Chemistry, University of Agriculture, Faisalabad 38000, Pakistan; [orcid.org/0000-0002-2446-6740](https://orcid.org/0000-0002-2446-6740)

**Mohamed Shaban** – Department of Physics, Faculty of Science, Islamic University of Madinah, Madinah 42351, Saudi Arabia; Nanophotonics and Applications (NPA) Lab, Physics Department, Faculty of Science, Beni-Suef University, Beni-Suef 62514, Egypt; [orcid.org/0000-0002-4368-8269](https://orcid.org/0000-0002-4368-8269)

**Shanza Hameed** – Department of Chemistry, University of Agriculture, Faisalabad 38000, Pakistan

**Ateeq-ur-Rehman** – Department of Physics, University of Agriculture, Faisalabad 38000, Pakistan

**H. A. Alrafai** – Department of Chemistry, College of Science, King Khalid University, Abha 61421, Saudi Arabia

**Sameerah I. Al-Saeedi** – Department of Chemistry, Collage of Science, Princess Nourah Bint Abdulrahman University, Riyadh 11671, Saudi Arabia

**Mahmoud A. A. Ibrahim** – Chemistry Department, Faculty of Science, Minia University, Minia 61519, Egypt; School of Health Sciences, University of KwaZulu-Natal, Durban 4000, South Africa; [orcid.org/0000-0003-4819-2040](https://orcid.org/0000-0003-4819-2040)

**N. M. A. Hadia** – Physics Department, College of Science, Jouf University, Sakaka 2014 Al-Jouf, Saudi Arabia

Complete contact information is available at:

<https://pubs.acs.org/10.1021/acsomega.3c04970>

## Notes

The authors declare no competing financial interest.

## ACKNOWLEDGMENTS

The authors extend their appreciation to the Deanship of Scientific Research at King Khalid University for funding this work through Larg Groups Project under grant number RGP.2/3/44. The authors express their gratitude to Princess Nourah bint Abdulrahman University Researchers Supporting Project number (PNURSP2024R58), Princess Nourah bint Abdulrahman University, Riyadh, Saudi Arabia.

## REFERENCES

- (1) Sun, Y.; et al. Flexible organic solar cells: progress and challenges. *Small Sci.* **2021**, *1* (5), No. 2100001.
- (2) Sadiq, S.; et al. Synergistic modification of end groups in Quinoxaline fused core-based acceptor molecule to enhance its photovoltaic characteristics for superior organic solar cells. *Journal of Molecular Graphics and Modelling* **2023**, *123*, No. 108518.
- (3) Wang, C.; Zhang, X.; Hu, W. Organic photodiodes and phototransistors toward infrared detection: materials, devices, and applications. *Chem. Soc. Rev.* **2020**, *49* (3), 653–670.
- (4) Hussain, K. *Kinetic Monte Carlo Investigation of Organic Solar Cell Architecture*; Technische Universität München, 2022.
- (5) Wang, J.; et al. The principles, design and applications of fused-ring electron acceptors. *Nature Reviews Chemistry* **2022**, *6* (9), 614–634.
- (6) Jiang, M.; et al. Rational compatibility in a ternary matrix enables all-small-molecule organic solar cells with over 16% efficiency. *Energy Environ. Sci.* **2021**, *14* (7), 3945–3953.
- (7) Maqsood, M. H.; et al. End-cap modeling on the thienyl-substituted benzodithiophene trimer-based donor molecule for achieving higher photovoltaic performance. *Journal of Molecular Graphics and Modelling* **2023**, *124*, No. 108550.
- (8) Janjua, M. R. S. A.; et al. Machine-Learning Analysis of Small-Molecule Donors for Fullerene Based Organic Solar Cells. *Energy Technol.* **2022**, *10* (5), No. 2200019.
- (9) Shen, Q.; et al. Design of Non-fused Ring Acceptors toward High-Performance, Stable, and Low-Cost Organic Photovoltaics. *Accounts of Materials Research* **2022**, *3* (6), 644–657.
- (10) Sharma, A.; et al. Flexible solar and thermal energy conversion devices: Organic photovoltaics (OPVs), organic thermoelectric generators (OTEGs) and hybrid PV-TEG systems. *Applied Materials Today* **2022**, *29*, No. 101614.
- (11) Kim, M. S.; et al. High-Sensitivity Organic Photodetector Based on Surface-Concentrated Nonfused Ring Electron Acceptor. *Adv. Opt. Mater.* **2023**, *11* (5), No. 2202525.
- (12) Zhao, J.; et al. Highly efficient non-fused-ring electron acceptors enabled by the conformational lock and structural isomerization effects. *ACS Appl. Mater. Interfaces* **2021**, *13* (21), 25214–25223.
- (13) Luo, D.; et al. Simultaneous Tuning of Alkyl Chains and End Groups in Non-fused Ring Electron Acceptors for Efficient and Stable Organic Solar Cells. *ACS Appl. Mater. Interfaces* **2022**, *14* (21), 24374–24385.
- (14) Kim, M. S.; et al. High-Sensitivity Organic Photodetector Based on Surface-Concentrated Nonfused Ring Electron Acceptor. *Adv. Opt. Mater.* **2022**, *11*, No. 2202525.
- (15) Janjua, M. R. S. A. All-small-molecule organic solar cells with high fill factor and enhanced open-circuit voltage with 18.25% PCE: Physical insights from quantum chemical calculations. *Spectrochimica Acta Part A: Molecular and Biomolecular Spectroscopy* **2022**, *279*, No. 121487.
- (16) Liang, X.; et al. The evolution of small molecular acceptors for organic solar cells: Advances, challenges and prospects. *Dyes Pigm.* **2022**, *198*, No. 109963.
- (17) Mishra, A.; Sharma, G. D. Harnessing the Structure-Performance Relationships in Designing Non-Fused Ring Acceptors for Organic Solar Cells. *Angew. Chem., Int. Ed.* **2023**, *62*, No. e202219245.

- (18) Rafiq, M.; et al. End-capped modification of dithienosilole based small donor molecules for high performance organic solar cells using DFT approach. *J. Mol. Liq.* **2022**, *345*, No. 118138.
- (19) Waqas, M.; et al. Theoretical framework for achieving high Voc in non-fused non-fullerene terthiophene-based end-capped modified derivatives for potential applications in organic photovoltaics. *RSC Adv.* **2023**, *13* (11), 7535–7553.
- (20) Rani, M.; et al. Novel A- $\pi$ -D- $\pi$ -A type non-fullerene acceptors of dithienyl diketopyrrolopyrrole derivatives to enhance organic photovoltaic applications: a DFT study. *RSC Adv.* **2023**, *13* (3), 1640–1658.
- (21) Yang, J.; et al. Theoretical study of non-fullerene acceptors using end-capped groups with different electron-withdrawing abilities toward efficient organic solar cells. *J. Phys. Chem. Lett.* **2022**, *13* (3), 916–922.
- (22) Basha, B.; et al. Multidimensional modelling and designing of efficient small molecule acceptors for organic solar cells. *Materials Science and Engineering: B* **2023**, *296*, No. 116618.
- (23) Singh, S. P.; et al. Synthesis of a Modified PC70BM and Its Application as an Electron Acceptor with Poly(3-hexylthiophene) as an Electron Donor for Efficient Bulk Heterojunction Solar Cells. *Adv. Funct. Mater.* **2012**, *22* (19), 4087–4095.
- (24) Nagarjuna, P.; et al. A highly efficient PTB7-Th polymer donor bulk hetero-junction solar cell with increased open circuit voltage using fullerene acceptor CN-PC70BM. *Org. Electron.* **2017**, *43*, 262–267.
- (25) Luo, D.; et al. Dual-functional ambipolar non-fused ring electron acceptor as third component and designing similar molecular structure between two acceptors for high-performance ternary organic solar cells. *Nano Energy* **2022**, *98*, No. 107186, DOI: 10.1016/j.nanoen.2022.107186.
- (26) Asif, A.; et al. Efficient side-chain engineering of thienoimidazole salt-based molecule to boost the optoelectronic attributes of organic solar cells: A DFT approach. *Journal of Molecular Graphics and Modelling* **2023**, *121*, No. 108428.
- (27) Rani, S.; et al. Designing dibenzosilole core based, A2- $\pi$ -A1- $\pi$ -D- $\pi$ -A1- $\pi$ -A2 type donor molecules for promising photovoltaic parameters in organic photovoltaic cells. *RSC Adv.* **2022**, *12* (45), 29300–29318.
- (28) Khan, M. I.; et al. Novel A- $\pi$ -D- $\pi$ -A-type non-fullerene acceptors for solution-processed organic photovoltaic cells: a DFT study. *J. Solid State Chem.* **2023**, *317*, No. 123714.
- (29) Rafiq, M.; et al. End-capped modification of dithienosilole based small donor molecules for high performance organic solar cells using DFT approach. *J. Mol. Liq.* **2022**, *345*, No. 118138.
- (30) Frisch, A. *gaussian 09W Reference: Wallingford, USA*, 2009; vol 470.
- (31) Dennington, R.; Keith, T.A.; Millam, J.M. *GaussView 6.0. 16*; Semichem Inc.: Shawnee Mission, KS, USA, 2016; p 25.
- (32) Finley, J. P. Using the local density approximation and the LYP, BLYP and B3LYP functionals within reference-state one-particle density-matrix theory. *Mol. Phys.* **2004**, *102* (7), 627–639.
- (33) Latosinska, J. N.; et al. Conformational stability and thermal pathways of relaxation in triclosan (Antibacterial/Excipient/Contaminant) in solid-state: combined spectroscopic (<sup>1</sup>H NMR) and computational (periodic DFT) study. *J. Phys. Chem. A* **2015**, *119* (20), 4864–4874.
- (34) Beerepoot, M. T.; et al. Benchmarking two-photon absorption cross sections: performance of CC2 and CAM-B3LY. *Phys. Chem. Chem. Phys.* **2015**, *17* (29), 19306–19314.
- (35) Zhang, G.; Musgrave, C. B. Comparison of DFT methods for molecular orbital eigenvalue calculations. *J. Phys. Chem. A* **2007**, *111* (8), 1554–1561.
- (36) Chai, J.-D.; Head-Gordon, M. Long-range corrected hybrid density functionals with damped atom–atom dispersion corrections. *Phys. Chem. Chem. Phys.* **2008**, *10* (44), 6615–6620.
- (37) Khan, M. U.; et al. Designing star-shaped subphthalocyanine-based acceptor materials with promising photovoltaic parameters for non-fullerene solar cells. *ACS omega* **2020**, *5* (36), 23039–23052.
- (38) Irfan, A.; Mahmood, A. Computational designing of low energy gap small molecule acceptors for organic solar cells. *J. Mex. Chem. Soc.* **2017**, *61* (4), 309–316.
- (39) Deschenes, L. A.; Vanden Bout, D. A. *Origin 6.0: Scientific Data Analysis and Graphing Software Origin Lab Corporation (formerly Microcal Software, Inc.)*. Web site: [www.originlab.com](http://www.originlab.com). Commercial price: \$95. Academic price: \$446; University of Texas, ACS Publications, 2000.
- (40) Tenderholt, A. L. *PyMOLyze: A Program to Analyze Quantum Chemistry Calculations*, 2019, Version.
- (41) Khan, M. I.; et al. End-capped group modification on cyclopentadithiophene based non-fullerene small molecule acceptors for efficient organic solar cells; a DFT approach. *Journal of Molecular Graphics and Modelling* **2022**, *113*, No. 108162.
- (42) Lu, T.; Chen, F. Multiwfn: A multifunctional wavefunction analyzer. *Journal of computational chemistry* **2012**, *33* (5), 580–592.
- (43) Zubair, I.; et al. Tuning the optoelectronic properties of indacenodithiophene based derivatives for efficient photovoltaic applications: a DFT approach. *Chem. Phys. Lett.* **2022**, *793*, No. 139459.
- (44) Abbas, M.; et al. Spirofluorene based small molecules as an alternative to traditional non-fullerene acceptors for organic solar cells. *Opt. Quantum Electron.* **2021**, *53* (5), 246.
- (45) O'Boyle, N. M.; Campbell, C. M.; Hutchison, G. R. Computational design and selection of optimal organic photovoltaic materials. *J. Phys. Chem. C* **2011**, *115* (32), 16200–16210.
- (46) Lin, B. C.; Cheng, C.; Lao, Z. P. M. Reorganization energies in the transports of holes and electrons in organic amines in organic electroluminescence studied by density functional theory. *J. Phys. Chem. A* **2003**, *107* (26), 5241–5251.
- (47) Bano, N.; et al. A DFT study of nonlinear optical response of supersalt (Al (BH<sub>4</sub>)<sub>3</sub>) doped boron nitride. *Journal of Taibah University for Science* **2022**, *16* (1), 621–631.
- (48) Saeed, M. U.; et al. End-capped modification of Y-Shaped dithienothiophen [3, 2-b]-pyrrolobenzothiadiazole (TPBT) based non-fullerene acceptors for high performance organic solar cells by using DFT approach. *Surfaces and Interfaces* **2022**, *30*, No. 101875.
- (49) Mahmood, A.; et al. First-principles theoretical designing of planar non-fullerene small molecular acceptors for organic solar cells: manipulation of noncovalent interactions. *Phys. Chem. Chem. Phys.* **2019**, *21* (4), 2128–2139.
- (50) Majeed, M.; et al. Modified optoelectronic parameters by end-group engineering of A-D-A type non-fullerene-based small symmetric acceptors constituting IBDT core for high-performance photovoltaics. *J. Phys. Chem. Solids* **2023**, *181*, No. 111495.
- (51) Majeed, M.; et al. Exploring the Electronic, Optical, and Charge Transfer Properties of A-D-A-Type IDTV-ThIC-Based Molecules To Enhance Photovoltaic Performance of Organic Solar Cells. *ACS Omega* **2023**, *8*, 45384 DOI: 10.1021/acsomega.3c04437.
- (52) Saeed, M. U.; et al. Impact of end-group modifications and planarity on BDP-based non-fullerene acceptors for high-performance organic solar cells by using DFT approach. *J. Mol. Model.* **2022**, *28* (12), 397.
- (53) Ishtiaq, M.; et al. Theoretical designing of symmetrical non-fullerene acceptor molecules by end-capped modification for promising photovoltaic properties of organic solar cells. *J. Mol. Liq.* **2023**, *386*, No. 122473.
- (54) Zahoor, A.; et al. A DFT study for improving the photovoltaic performance of organic solar cells by designing symmetric non-fullerene acceptors by quantum chemical modification on pre-existed LC81 molecule. *Journal of Molecular Graphics and Modelling* **2023**, *125*, No. 108613.
- (55) Akram, M.; et al. End-capped engineering of bipolar diketopyrrolopyrrole based small electron acceptor molecules for high performance organic solar cells. *Computational and Theoretical Chemistry* **2021**, *1201*, No. 113242.
- (56) Zahid, S.; et al. Tuning the optoelectronic properties of triphenylamine (TPA) based small molecules by modifying central core for photovoltaic applications. *J. Mol. Model.* **2021**, *27*, 237.

- (57) Uzun, K. K.; Sayin, S.; Çevik, U. Electronic structure and photophysical properties of some promising organic molecules for organic solar cells. *J. Mol. Model.* **2023**, *29* (10), 323.
- (58) Khan, M. U.; et al. Designing Electron-Deficient Diketone Unit Based Non-Fused Ring Acceptors with Amplified Optoelectronic Features for Highly Efficient Organic Solar Cells: A DFT Study. *Molecules* **2023**, *28* (8), 3625.
- (59) Rasool, A.; et al. Bithieno thiophene-based small molecules for application as donor materials for organic solar cells and hole transport materials for perovskite solar cells. *ACS omega* **2022**, *7* (1), 844–862.
- (60) Fu, Y.; et al. Molecular orientation-dependent energetic shifts in solution-processed non-fullerene acceptors and their impact on organic photovoltaic performance. *Nat. Commun.* **2023**, *14* (1), 1870.
- (61) Kumer, A.; Sarker, M. N.; Paul, S. The thermo physical, HOMO, LUMO, Vibrational spectroscopy and QSAR study of morphonium formate and acetate Ionic Liquid Salts using computational method. *Turkish Computational and Theoretical Chemistry* **2019**, *3* (2), 59–68.
- (62) Zubair, H.; et al. Effect of tailoring  $\pi$ -linkers with extended conjugation on the SJ-IC molecule for achieving high VOC and improved charge mobility towards enhanced photovoltaic applications. *RSC Adv.* **2023**, *13* (37), 26050–26068.
- (63) Zahid, S.; et al. Tuning the optoelectronic properties of triphenylamine (TPA) based small molecules by modifying central core for photovoltaic applications. *J. Mol. Model.* **2021**, *27* (9), 237.
- (64) Waqas, M.; et al. Theoretical framework for achieving high Voc in non-fused non-fullerene terthiophene-based end-capped modified derivatives for potential applications in organic photovoltaics. *RSC Adv.* **2023**, *13* (11), 7535–7553.
- (65) Liu, H.; Liu, X. Strategy to modulate the  $\pi$ -bridged units in bis (4-methoxyphenyl) amine-based hole-transporting materials for improvement of perovskite solar cell performance. *Journal of Materials Chemistry C* **2018**, *6* (25), 6816–6822.
- (66) Ahmadi, R.; Soleymani, R.; Yousofzad, T. Study on effect of addition of nicotine on nanofullerene structure C60 as a medicine nano carrier. *Orient. J. Chem.* **2012**, *28* (2), 773.
- (67) Chi, W.-J.; Li, Q.-S.; Li, Z.-S. Exploring the electrochemical properties of hole transport materials with spiro-cores for efficient perovskite solar cells from first-principles. *Nanoscale* **2016**, *8* (11), 6146–6154.
- (68) Akram, W.; et al. Engineering push–pull structural versatility in highly functional carbazole-based hole transporting materials design for efficient perovskites solar devices. *J. Photochem. Photobiol., A* **2023**, *444*, No. 114991.
- (69) Risko, C.; McGehee, M. D.; Brédas, J.-L. A quantum-chemical perspective into low optical-gap polymers for highly-efficient organic solar cells. *Chemical Science* **2011**, *2* (7), 1200–1218.
- (70) Joseph, S.; Ravva, M. K.; Bredas, J.-L. Charge-transfer dynamics in the lowest excited state of a pentacene–fullerene complex: implications for organic solar cells. *J. Phys. Chem. Lett.* **2017**, *8* (20), 5171–5176.
- (71) Ahmed, S.; Dutta, R.; Kalita, D. J. Strategical designing of diketopyrrolopyrrole-thiophene based donor-acceptor type organic oligomers and study their transport properties: A DFT/TD-DFT perspective. *Chem. Phys. Lett.* **2019**, *730*, 14–25.
- (72) Wu, C.; Tretiak, S.; Chernyak, V. Y. Excited states and optical response of a donor–acceptor substituted polyene: A TD-DFT study. *Chemical physics letters* **2007**, *433* (4–6), 305–311.
- (73) Park, Y.; et al. A new pH sensitive fluorescent and white light emissive material through controlled intermolecular charge transfer. *Chemical science* **2015**, *6* (1), 789–797.
- (74) Masood, T. B. et al. Visual analysis of electronic densities and transitions in molecules. In *Computer Graphics Forum*; Wiley Online Library, 2021.
- (75) Ali, R.; et al. An Approach Towards Low Energy Loss by End-capped Modification of A2–D–A1–D–A2-type Molecules for Tuning the Photovoltaic Properties of Organic Solar Cells. *J. Comput. Biophys. Chem.* **2023**, *22*, 1–28.
- (76) Waqas, M.; et al. End-group modification of terminal acceptors on benzothiadiazole-based BT2F-IC4F molecule to establish efficient organic solar cells. *J. Mol. Liq.* **2022**, *368*, No. 120770.
- (77) Sharif, A.; et al. Tuning the optoelectronic properties of dibenzochrycene (DBC) based small molecules for organic solar cells. *Materials Science in Semiconductor Processing* **2021**, *127*, No. 105689.
- (78) Aslam, M. R.; et al. Tuning of diphenylamine subphthalocyanine based small molecules with efficient photovoltaic parameters for organic solar cells. *Journal of Molecular Graphics and Modelling* **2022**, *112*, No. 108146.
- (79) Rayene, K.; et al. Molecular modeling study of structures, Hirschfeld surface, NBO, AIM, RDG, IGM and 1HNMR of thymoquinone/hydroxypropyl- $\beta$ -cyclodextrin inclusion complex from QM calculations. *J. Mol. Struct.* **2022**, *1249*, No. 131565, DOI: 10.1016/j.molstruc.2021.131565.
- (80) Priscilla, J.; et al. Experimental and theoretical spectroscopic analysis, hydrogen bonding, reduced density gradient and antibacterial activity study on 2-Phenyl quinoline alkaloid. *Chem. Phys.* **2020**, *536*, No. 110827, DOI: 10.1016/j.chemphys.2020.110827.
- (81) Rehman, F. U.; et al. High-Efficiency and Low-Energy-Loss Organic Solar Cells Enabled by Tuning the End Group Modification of the Terthiophene-Based Acceptor Molecules to Enhance Photovoltaic Properties. *ACS Omega* **2023**, *8* (45), 42492–42510.
- (82) Kazachenko, A. S.; et al. Intermolecular hydrogen bonds interactions in water clusters of ammonium sulfamate: FTIR, X-ray diffraction, AIM, DFT, RDG, ELF, NBO analysis. *J. Mol. Liq.* **2021**, *342*, No. 117475.
- (83) Yan, J.; et al. Identifying structure–absorption relationships and predicting absorption strength of non-fullerene acceptors for organic photovoltaics. *Energy Environ. Sci.* **2022**, *15* (7), 2958–2973.
- (84) Waqas, M.; et al. Impact of end-capped modification of MO-IDT based non-fullerene small molecule acceptors to improve the photovoltaic properties of organic solar cells. *Journal of Molecular Graphics and Modelling* **2022**, *116*, No. 108255.
- (85) Zubair, H.; et al. A computational insight into enhancement of photovoltaic properties of non-fullerene acceptors by end-group modulations in the structural framework of INPIC molecule. *Journal of Molecular Graphics and Modelling* **2024**, *126*, No. 108664.
- (86) Waqas, M.; et al. Designing of symmetrical ADA type non-fullerene acceptors by side-chain engineering of an indacenodithienothiophene (IDTT) core based molecule: A computational approach. *Computational and Theoretical Chemistry* **2022**, *1217*, No. 113904.
- (87) Hassan, A. U.; et al. Enriching the compositional tailoring of NLO responsive dyes with diversity oriented electron acceptors as visible light harvesters: a DFT/TD-DFT approach. *Mol. Phys.* **2022**, *121*, No. e2148585.
- (88) Idrees, A.; et al. Strategies Toward End-group Engineering of Chrysenes Core-based Non-fullerene Acceptors for High Performance Organic Solar Cells: A DFT Study. *J. Comput. Biophys. Chem.* **2023**, *22*, 1041–1066.
- (89) Rehman, F. U.; et al. Approach toward Low Energy Loss in Symmetrical Nonfullerene Acceptor Molecules Inspired by Insertion of Different  $\pi$ -Spacers for Developing Efficient Organic Solar Cells. *ACS. Omega* **2023**, *8* (46), 43792–43812.
- (90) Sathya, B.; Prasath, M. Spectroscopic (FT-IR, FT-Raman, UV–Vis), quantum chemical calculation and molecular docking evaluation of liquiritigenin: an influenza A (H1N1) neuraminidase inhibitor. *Res. Chem. Intermed.* **2019**, *45*, 2135–2166.
- (91) Ans, M.; et al. Spirobifluorene based small molecules as an alternative to traditional fullerene acceptors for organic solar cells. *Materials Science in Semiconductor Processing* **2019**, *94*, 97–106.
- (92) Nagasundaram, N.; et al. Synthesis, characterization and biological evaluation of novel azo fused 2, 3-dihydro-1H-perimidine derivatives: In vitro antibacterial, antibiofilm, anti-quorum sensing, DFT, in silico ADME and Molecular docking studies. *J. Mol. Struct.* **2022**, *1248*, No. 131437.
- (93) Qaisar, M.; et al. Molecular Modeling of Pentacyclic Aromatic Bislactam-Based Small Donor Molecules by Altering Auxiliary End-

Capped Acceptors to Elevate the Photovoltaic Attributes of Organic Solar Cells. *ACS omega* **2022**, *7* (24), 20528–20541.

(94) Zheng, B.; et al. Quantum criticality of excitonic Mott metal-insulator transitions in black phosphorus. *Nat. Commun.* **2022**, *13* (1), 7797.

(95) Cai, X.; Su, S. J. Marching toward highly efficient, pure-blue, and stable thermally activated delayed fluorescent organic light-emitting diodes. *Adv. Funct. Mater.* **2018**, *28* (43), No. 1802558.

(96) Rashid, E. U.; et al. Depicting the role of end-capped acceptors to amplify the photovoltaic properties of benzothiadiazole core-based molecules for high-performance organic solar cell applications. *Comput. Theor. Chem.* **2022**, *1211*, No. 113669.

(97) He, Y.; et al. Defect engineering of photocatalysts for solar-driven conversion of CO<sub>2</sub> into valuable fuels. *Mater. Today* **2021**, *50*, 358–384.

(98) Yousaf, I.; et al. Isatin-derived non-fullerene acceptors for efficient organic solar cells. *Materials Science in Semiconductor Processing* **2021**, *121*, No. 105345.

(99) Khan, M. U.; et al. Molecular designing of high-performance 3D star-shaped electron acceptors containing a truxene core for nonfullerene organic solar cells. *J. Phys. Org. Chem.* **2021**, *34* (1), No. e4119.

(100) Park, S.; et al. The origin of high PCE in PTB7 based photovoltaics: proper charge neutrality level and free energy of charge separation at PTB7/PC71BM interface. *Sci. Rep.* **2016**, *6* (1), 35262.

(101) Yaqoob, U.; et al. Structural, optical and photovoltaic properties of unfused Non-Fullerene acceptors for efficient solution processable organic solar cell (Estimated PCE greater than 12.4%): A DFT approach. *J. Mol. Liq.* **2021**, *341*, No. 117428.

(102) Zahid, H.; et al. Designing phenyl-di-p-tolyl-amine-based asymmetric small molecular donor materials with favorable photovoltaic parameters. *Optik* **2022**, *256*, No. 168739, DOI: [10.1016/j.ijleo.2022.168739](https://doi.org/10.1016/j.ijleo.2022.168739).

(103) Zara, Z.; et al. Designing dibenzosilole and methyl carbazole based donor materials with favourable photovoltaic parameters for bulk heterojunction organic solar cells. *Computational and Theoretical Chemistry* **2018**, *1142*, 45–56.